POLITECNICO DI TORINO

Master's Degree in Energy and Nuclear Engineering

Master's Degree Thesis

Aging and electrochemical-thermal model of lithium-ion batteries

Supervisors

Prof. MASSIMO SANTARELLI

Prof. SILVIA BODOARDO

Candidate

STEFANIA PICHIERRI

LUGLIO 2021

Abstract

Abstract

Nowadays, with the deployment of clean technologies, in order to reduce air pollution and greenhouse gas emissions, energy storage technologies play an important role in energy transition. Electrical Energy Storages (EES) convert energy from one form, usually electrical one, to another form, storing it in various medium. When users need energy, it is converted back in electricity.

Battery electric vehicles (BEV) are integrated in a lot of cities as a result of legislative measures taken to reduce environment pollution. This work is focused on high energy density lithium-ion batteries, suitable for automotive sector. The high capacity cathode taken into account is $Ni_{0.6}Mn_{0.6}Co_{0.2}O_2$, instead two types of anode are exploited, graphite, one of the most common carbonaceous anode material, and lithium metal, for the lowest redox potential (-3.040 V vs standard hydrogen electrode) and its considerable capacity (3860 mAh g^{-1}).

In particular, the work is divided into two parts. The former has the aim to evaluate, both for graphite/NMC622 and lithium/NMC622, capacity fade and degradation mechanisms over storage periods. Ageing mechanisms are investigated alternating an electrochemical characterization procedure with storage periods. The goal is to collect data on ageing at different storage conditions. The procedure is composed of 4 steps, a capacity test, a micro rate test, a pulse test and an electrochemical impedance spectroscopy test. The impedance curve obtained is fitted by an equivalent circuit, determining parameters of the circuit model. These parameters will give information about ageing states and capacity fade.

The second part is the implementation of an electrochemical and thermal model using a finite element package *Comsol Multiphysics 5.5*, an useful tool to gain insights to cells internal phenomena, forecast their operation and optimize cell design parameters. The approach used in this study is the P2D model, giving the possibility of putting micro and macro scale together. Micro scale processes are related to diffusion through active material surface. Instead, macro scale phenomena are connected to transfer processes, predominantly, unidirectional. These two realms are linked by law of species conservation. Exothermic reactions occurring inside cell generate a system over heating, causing dangerous thermal runaways, faster ageing and capacity fade. In order to avoid these unwanted

phenomena and better design the batteries, a 3D thermal model has been coupled to P2D electrochemical model. This final model has been validated with cells assembled in laboratory. Such an accurate model could be used as predictive instrument to reduce the number of experiments.

This work was part of the project THERMODEL BAT "Development of innovative thermal model to predict ageing of high energy batteries for EVs" between Stellantis and Politecnico di Torino.

Table of Contents

List of Tables

List of Figures

Acronyms

BEV

Battery Electric Vehicle

BMS

Battery Management System

CAES

Compressed Air Energy Storage

DOD

Depth of discharge

EEC

Electrical Equivalent Circuit

EES

Electrical energy storage

EFC

Equivalent full cycle

EIS

Electrochemical Impedance Spectroscopy

EV

Electrical vehicles

GITT

galvanostatic intermittent titration technique

ICE

Internal Combustion Engine

KMC

Kinetic Monte Carlo

LCO

Lithium Cobalt Oxide

LMO

Lithium Manganese Oxide

NMC

Nickel Manganese Cobalt

OCV

Open Circuit Voltage

P2D

Pseudo Two Dimensional

PHES

Pumped Hydroelectric Energy Storage

RES

Renewable energy system

SEI

Solid electrolyte interface

SMES

Superconducting magnetic energy storage

SOC

State of charge

SPM

Single Particle Model

Chapter 1

Introduction

Nowadays, power generation is dramatically changing due to the need to reduce environmental pollution and greenhouse gas emissions. Factories based on fossil fuel and internal combustion engine (ICE) vehicles are the main causes of CO_2 emissions and global warming. These targets could be achieved increasing the use of renewable energy systems (RESs), but some of those are susceptible to daily and seasonal variations such as wind or solar energy. Researchers are turned towards electrical energy storage (EESs), which are a good solution to ensure electrical energy when it is needed [1]. In fact, this technology converts energy from one form, usually electrical one, to another form, storing it in various medium. When users need energy, it is converted back in electricity.
One of the first and most common storage technology is pumped hydroelectric energy storage (PHES) [2] which use the difference in altitude of two reservoirs. Currently, new and advanced systems have been designed. Compressed air energy storage (CAES), chemical batteries, flywheels, super capacitors, load acid, superconducting magnetic energy storage (SMES) and so on. An overview of the main EESs and a comparison between them is displayed in the Ragone plot, Fig. 1.1.
Battery market is undergoing a large expansion due to the increasing demand of electrical vehicles (EVs), mobile devices and energy storage systems. Lithium-ion batteries, for example, are considered one of the most promising energy conversion and storage devices due to their high energy density, high efficiency, superior rate capability and long cycling life with respect to other kind of batteries [3].

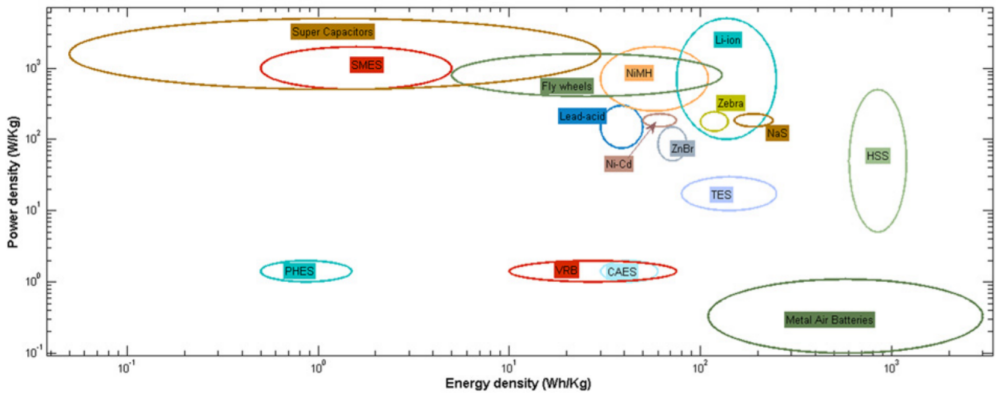

Figure 1.1: Comparison of different storage technologies

1.1 Principle of Lithium-Ion batteries

The energy storage mechanism of lithium-ion batteries is quite linear. The energy is stored in negative and positive electrode made of lithium-intercalation (or insertion) compounds in which oxidation and reduction reactions occur. These two are electrically insulated from each other by a separator. A medium conducting only lithium ions (*electrolyte*) is placed in between the two electrodes, it may be a liquid, a gel, a solid polymer or an inorganic solid; whereas electrons generated from the reaction pass through an external circuit to do work. An illustration of a lithium-ion battery may be seen in Fig. 3.11.

In general, during discharge the negative electrode is referred as *anode* and the positive electrode as *cathode*, but during charge phase the names are interchanged, therefore for reducing misunderstanding, in this work positive and negative terminology has been adopted.
The lithium insertion into negative electrode occurs during charging at higher voltages than lithium deposition. The issues related to lithium deposition will be seen later.
The charge and discharge reactions taking place at graphite electrode, which is the most common negative electrode material, are shown below:

$$Li_{x-y}C_6 + yLi^+ + ye^- \overset{charge}{\Longrightarrow} Li_xC_6 \tag{1.1}$$

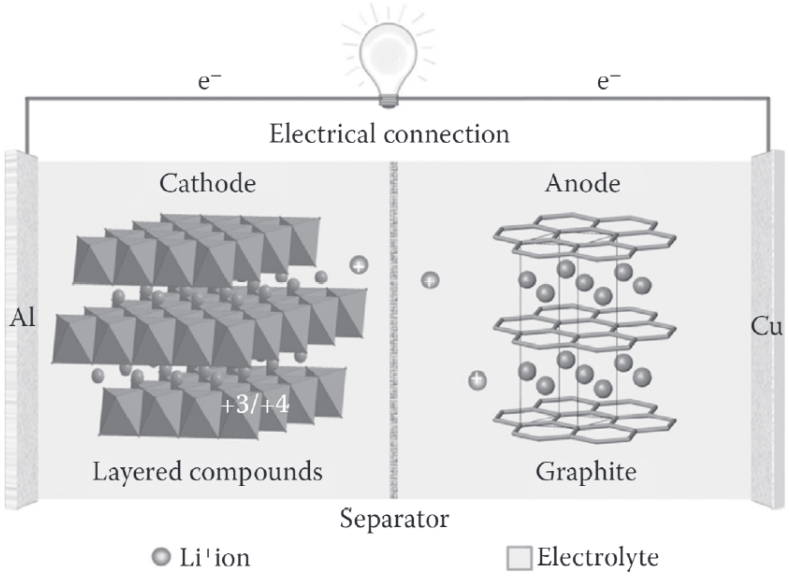

Figure 1.2: Representation of a lithium-ion battery

$$Li_xC_6 \overset{discharge}{\Longrightarrow} Li_{x-y}C_6 + yLi^+ + ye^- \tag{1.2}$$

The amount of lithium ions intercalating into graphite is extracted from the positive electrode during charging. Regarding positive electrode materials, high potential vs. Li^+/Li positive electrode are preferred, but actually the working potentials are often limited by electrolyte stability. The reactions at the positive side are:

$$Li_xMp \overset{charge}{\Longrightarrow} Li_{z-y}Mp + yLi^+ + ye^- \tag{1.3}$$

$$Li_{z-y}Mp + yLi^+ + ye^- \overset{discharge}{\Longrightarrow} Li_xMp \tag{1.4}$$

1.2 Anode materials

Historically, due to its low cost, great availability and possibilities of modification, carbon was used as anode in the first commercial Li-ion batteries. Alternative forms of carbon materials and new nanomaterials and their corresponding reaction mechanisms and surface effects have been investigated since the early 1990s [4].

Graphite is the most common anode material, the doping of graphite with lithium produces the graphite intercalation compounds whose formula is Li_xC_6(x<1). The substitution of lithium by a carbonaceous material as negative electrode led to the creation of the "rocking-chair" battery commercialized by Sony Corporation in 1991, avoiding the issues related to formation of dendrites and getting major safety. Moreover, the lower safety, linked to the much higher reactivity of Li metal, especially when cycled, remains a very difficult issue. Obviously, other metallic alloy were taken in account in order to substitute pure lithium but with little success. The first important problem run into is the volume variation between charge and discharge. This volume changing, unfortunately, produces solid electrolyte interface (SEI) grains fragmentation, hence an amount of cycling lithium is used to repair SEI. Some effects are capacity drop and poor cycle life [4].
Another issue is the working voltage of the new negative electrode versus Li metal. In most of the cases, the working potential is higher than Li, so the cell potential is reduced, which reduces the energy density.

1.2.1 Lithium metal as anode

Since li-ion batteries are widely used for portable electronic devices and are emerging into transportation and grid applications, it is interesting to look at alternative high-capacity anodes. Among these, lithium metal battery is a good option considering its ultra-high capacity (3860 mAh g^{-1}) and very low redox potential (-3.040 V vs standard hydrogen electrode). Keeping in mind that traditional graphite-anode-based li-ion batteries gets a limited specific capacity (the theoretical one is about 386 mAh g^{-1}) and have almost reached their theoretical specific energy density (350 Wh kg^{-1}) and these values are not enough to satisfy market's demand [5].
In spite of these advantages, unfortunately, there are still a lot of obstacles hindering this technology and its applications: dendrite growth, lithium metal high reactivity and infinite volume changes of Li metal. The low reduction potential of the metallic lithium makes it highly reactive, reducing almost every type of electrolyte on its surface, generating the solid electrolyte interface, SEI. Li passivation, made possible by the SEI, allows the cell to operate in a such reductive environment and extend the voltage window to 4 V and above. Anyway, SEI behaviour will be explain better in the next chapter.
The infinite volume change can break the fragile SEI during Li plating/stripping,

promoting the dendrite growth through the cracks. The uncontrolled dendrite growth could generate internal short-circuit, heat generation and, in the worst case, also battery explosion. During Li stripping, volume contraction further fractures the SEI, while stripping from kinks in a dendrite or from its roots can break the electrical contact and produce 'dead' Li, decreasing the coulombic efficiency and reducing the battery life, as well. After ongoing cycling, a porous Li electrode will be produced, with a thick accumulated SEI layer and excessive dead Li, leading to blocked ion transport and capacity fading [6]. Fig. 1.3 summarizes the processes explained above.
Some electrolyte additives, especially gaseous molecules, 2-methylfuran, organic aromatic compounds, vinylene carbonate and various surfactans, have been seen to improve the performance of Li anodes. A big challenge for researchers is to develop an advanced solid electrolyte to prevent dendrite growth and they can be divided mainly into two groups: inorganic ceramic electrolyte and solid polymer electrolyte. The first one gets a ionic conductivity also higher than most of liquid electrolyte but a consideration has to be made about elastic modulus and surface adhesion with Li metal. Inorganic ceramic electrolyte elastic module ranges from tens to hundreds of gigapascals, good for preventing dendrite growth. But, high-modulus materials do not often show a good adhesion, increasing interfacial resistance during cycling. Thus, a trade-off between these two aspects has to be done. Solid polymer electrolytes, on the other hand, present a lower ionic conductivity compared to liquid electrolyte and also a lower elastic modulus than ceramic. However, their adhesion is better and as well as polymer electrolytes exhibit a good flexibility [7]. Li metal battery is a field actively studied since this technology could bring significant advantages, as said before, considering also the rapid market evolution and high required performances.

1.3 Cathode materials

The basic difference among different kind of lithium-ion batteries is in the material used as cathode electrode, especially. In this section, an overview about different cathode materials is presented.
The traditional cathode material in lithium ion battery is $LiCoO_2$ (LCO) [8]. LCO is a good cathode material but it is not stable as other cathode materials and if

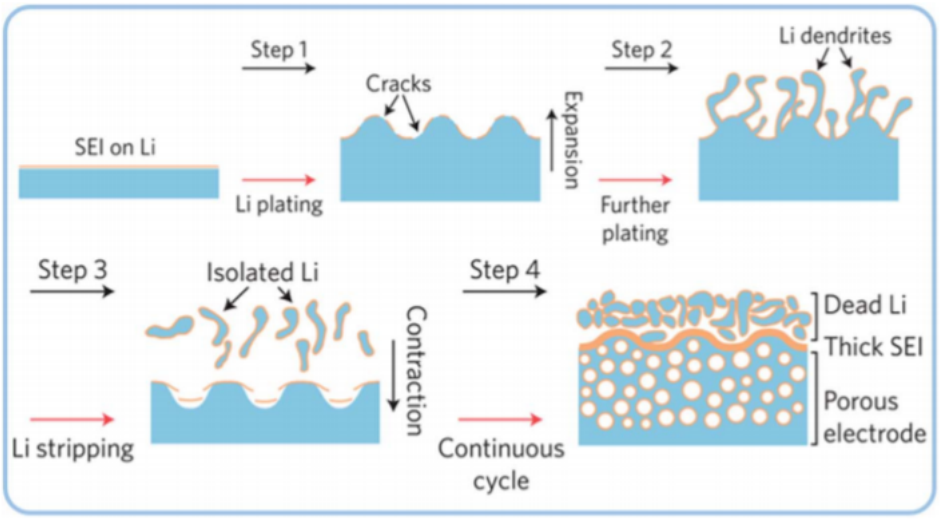

Figure 1.3: Dendrite growth and Li "dead" formation

overcharged could degrade, for these reasons some alternatives are being developed with a better stability and lower cost. Cobalt degradation is probably due to its dissolution in the electrolyte during charging, when the positive electrode is delithiated; as consequence during discharging less lithium manages to be intercalated [9]. In addition, a lattice parameter variation with changing in lithium concentration can lead to micro-cracking of the cathode particles. And finally, other transition metals are more available than cobalt, such as manganese, nickel and iron.
$LiNiO_2$, chemically, has the same structure of LCO and has a lower cost and an higher energy density, but is less stable and ordered. For increasing the degree of ordering, cobalt is added [10]. Thus, $LiNi_{1-x}Co_xO_2$, typically containing mostly nickel ($x \simeq 0.8$), has been used to take advantage of the low cost and higher capacity of nickel compared to cobalt.
$LiMnO_2$ has, instead, a monoclinic structure. Thanks to the addition of nickel or, in most cases, both nickel and cobalt, the same structure of previous ones is obtained [11]. The most commonly used $Li(Ni,Mn,Co)O_2$ composition contains equal amounts of the three transition metals, i.e. $Li(Ni_{1/3}Mn_{1/3}Co_{1/3})O_2$ (NMC), and has high capacity, good rate capability and can operate at high voltages. A higher charging voltage increases the capacity, but also leads to faster loss of capacity. Adding a major amount of cobalt helps to improve capacity, increasing the conductivity and improving the structural stability of the cathode. Although nickel

has been shown to stabilize the structure during delithiation and thus improve cycling performance.
Another promising cathode material is $LiMn_2O_4$, one of the most used oxide in LMO batteries, cheaper and safer than LCO, but with a lower capacity with respect to cathode materials described above. A challenge is the phase changes which can bump into during cycling.
Nickel is used to be added to $LiMn_2O_4$, which decreases the lattice parameter and the electrical conductivity of $LiMn_2O_4$. The capacity increases with increasing manganese content and a 3:1 Mn:Ni ratio is the most common in the market. $Li_xNi_{1-x}O$ can cause cell performance degradation, thus cobalt could be partially substitute nickel [12].
Other two type of cathode materials are V_2O_5 and LiV_3O_8. These electrodes have high capacities, but relatively low voltages (typically 3V or less). Another promising class of cathode materials are phosphates ($LiMPO_4$). The phosphate most commonly used for the cathode is $LiFePO_4$, which shows tolerance if overcharged and gets good performance along all SOC range; its specific energy is lower with respect to other materials and electronic conduction is relatively low (10^{-9} S cm^{-1} for pure $LiFePO_4$). Conductivity can be improved by heat treating to increase the hole conductivity, but the addition of a conductive phase is generally needed. Other phosphates used for cathodes are $LiMnPO_4$ and $LiCoPO_4$ which have higher open circuit voltages (4.1 and 4.8 V, respectively) than LiFePO4 (3.5 V), but have lower capacities. Also mixtures of phosphates, $LiMnPO_4$ or $LiCoPO_4$ with $LiFePO_4$, have been used. In such mixtures, the operating voltage increases with increasing manganese content, while capacity increases with increasing iron content [13].
A qualitative comparison between different technologies is shown in Fig. 1.4.

1.3.1 Focus on NMC

As said above, nowadays lithiated transition-metal oxides, $LiNi_xMn_yCo_zO_2$ (NMC) in particular, cobalt is partially replaced with nickel and manganese, are considered a new generation of cathode materials [14].
NMC622 is an interesting material (the numbers representing the relative amounts of each metal in the electrode), especially due to its high Ni content. Batteries with NMC cathode materials due to their excellent performance, high capacity and energy density, low cost, good stability and safety are a good option for electric

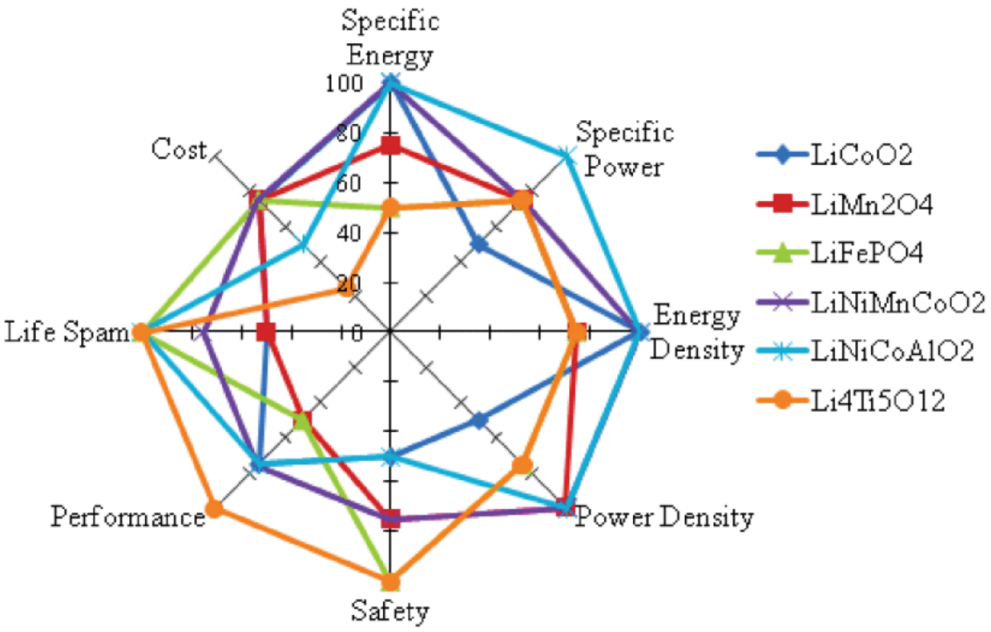

Figure 1.4: Qualitative comparison between different lithium-ion batteries

vehicles, portable power tools and electric energy storage system.
The nominal voltage of a NMC cell is 3.7 V and it is usually cycled from 2.5 V to 4.2 V, and vice versa. NMC111 and NMC532 are the most commercial compositions, but in this work the focus is on the innovative NMC622.

1.4 Batteries under study

In this work, the lithium-ion batteries have been assembled inside a MBraun UNIlab GloveBox, Fig. 1.5, full of Argon, with a oxygen and moisture concentration lower than 1 ppm, due to electrolyte high reactivity with oxygen.

1.4.1 Coin cell 2032

For the thesis work, ageing and model validation of lithium-ion batteries, coin cells 2032 have been tested. Fig. 1.6 shows a schematic representation of a coin cell. It is made up of, from the top: negative case, spring, spacer (0.5 mm of thickness), anode (graphite with copper current collector or lithium foil), liquid electrolyte

Figure 1.5: MBraun UNIlab GloveBox

EC:DEC 1:1 $LiPF_6$ 1M, commercial separator of polypropylene (Celgard 2325 for Graphite/NMC622 coin cells and Celgard 2500 for Lithium/NMC622), NMC622 as cathode with aluminum current collector, another spacer (always 0.5 mm of thickness) and, finally, the positive case.

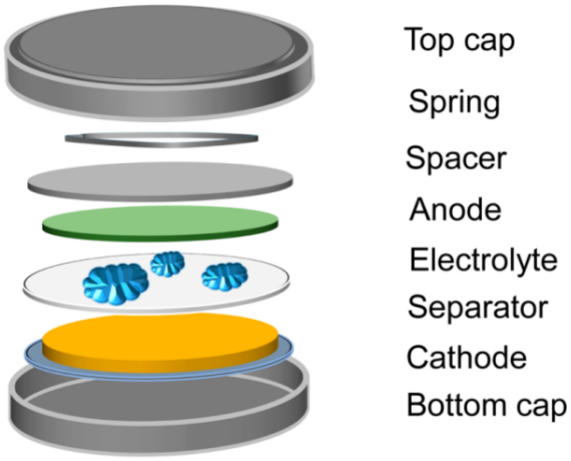

Figure 1.6: Schematic representation of a coin cell 2032

Graphite and NMC622 have been provided by CRF-Stellantis and have been obtained from batteries that have already worked. The roll of graphite, Fig. 3.14(a), is composed of: a graphite layer, the copper layer and another graphite layer. For coin cells assembly one of the graphite layer has been scratched away, trying to ruin as little as possible both copper collector and useful graphite. The same has been done with NMC622, Fig. 3.14(b), in between two NMC layers there is the aluminum collector.

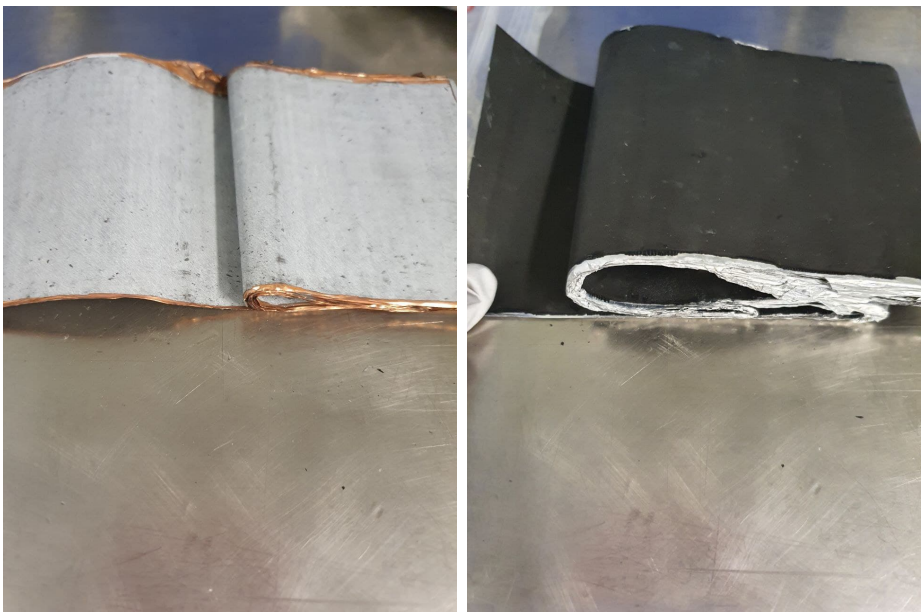

(a) Graphite (b) NMC622

Figure 1.7: Roll of graphite and NMC622

1.4.2 T-cell

T-cell consisting of a hydraulic connection in polypropylene, a inert material with respect to electrode and electrolyte, equipped with three 304 stainless steel cylinders with a diameter of 1 cm acting as electrical connections (current holder). All the main components can be put into this type of cell, according to the following layout: anode, separator soaked in electrolyte and cathode. T-cell gets the advantage of allowing the insertion of a third electrode which is the reference in impedance and cyclic voltammetry tests.

Figure 1.8: Scratching away a NMC622 layer

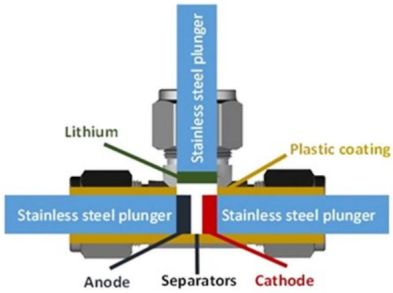

Figure 1.9: T-cell

1.5 Steps of the work

This work is subdivided into two parts, respectively is related to a specific topic, ageing and modelling.
The aim of the first part is to investigate the degradation mechanisms occurring in two types of lithium-ion batteries, graphite/NMC622 and lithium/NMC622. The common approach is to separate between calendar and cycle aging. The first one refers to degradation mechanisms during storage periods, the second one, instead, pertains to capacity fade during operation. In particular, the work is focused on calendar ageing; unfortunately cycle ageing study did not give good results because of use of poor quality material. The experimental procedure carried out to examine

calendar ageing, the tools used, as well as test results will be shown.
The second part of the work has the purpose of develop a thermo-electrochemical model for high energy density li-ion battery. This is a useful tool to design cells, in order to foresee polarization curves, capacity fade and thermal behaviour. To reach the goal a Pseudo 2D model has been chosen and the equations operating the model will be explained, followed by, description of the coupling between thermal and electrochemical model, the insertion of SEI layer in the general model, the equations employed to depict its growth over time and the effect of graphite particle expansion on it. SEI model has been implemented only for graphite/NMC622, due to lack of information in literature for modelling SEI film on metallic lithium surface. Successively, experimental tests performed to find model parameters out are illustrated. And finally, the model has been validated, comparing electrochemical and thermal results coming out from the model with experimental ones.

Part I

Experimental part

Chapter 2

Calendar ageing

In this chapter both experimental procedure performed to study calendar ageing and test results are reported.
The approach followed in this work is to distinguish between calendar and cycle ageing: the former refers to capacity fade during storage periods, while the second one refers to cell degradation during operation. The aging effects are measured in terms of capacity fade and power fade. Capacity fade refers to loss in discharge capacity that a battery demonstrates over time. Power fade is the decrease of the power capability caused by an increase in the internal resistance/impedance of the cell.

2.1 Ageing mechanism in lithium-ion batteries

The rapid advance of Li-ion batteries in the market of portable electronic devices, EVs, temporary storage systems for RESs and also in the market of batteries for conventional vehicles, requires an improvement of battery life-time. Unfortunately, lithium-ion batteries are complex systems to understand and the mechanisms of their ageing are even more complicated. Capacity decrease and power fading do not originate from one single cause, but from a number of various processes and their interactions. Ageing mechanisms occur differently at anodes and cathodes, hence are separately discussed.

2.1.1 Ageing of graphite

Electrode properties are subject to a modification due to ageing effects. These properties alteration may occur during storage, thus will affect the calendar life of the battery, or during working, that will influence the cycle life causing lithium metal plating or mechanical degradation. Calendar ageing can be monitored by electrochemical "values" such as capacity loss, impedance rise, potential change, SOC [15].
The main source for anode degradation, in accordance to many researches, is due to changes at the electrode/electrolyte interface by reactions of the anode with the electrolyte [16]. The low reduction potential of the graphite arouses the creation of a solid electrolyte interface (SEI) over first charging cycles, which passivates the anode's surface. In addition, SEI allows an extended battery life and inhibits further electrolyte reduction. But SEI is not entirely understood and it would appear to change its structure and composition over ageing [15].
The properties of the SEI layers are unique since they are permeable for lithium cations but rather impermeable for other electrolyte components and electrons. In fact, SEI layer protects electrolyte compounds from further reduction and electrode from corrosion. Of course, a certain amount of irreversible charge capacity is exhausted in order to build SEI layer and the capacity lost is seen to be dependent on the specific surface area of the graphite as well as on the layer formation conditions [17]. Moreover, other charged and neutral species seems to diffuse through SEI and as a consequence, corrosion of Li_xC_6 and electrolyte decomposition can be seen throughout the entire battery life [15]. Obviously, it follows that other electrolyte is lost and additional SEI is formed. On a long time scale, the SEI penetrates into electrode pores and, sometimes, into separator pores, causing a decrease of the accessible active area of the electrode.
As said above, monitoring some electrochemical values helps to understand what happens inside the cell. As an example, an increase in electrode impedance is considered to be caused by the growth of the SEI as well as by changes of the SEI in composition and morphology. Another important factor is the SEI thermal behaviour. It is believed, in fact, that the morphology and composition of the SEI changes at elevated temperatures [18]. In the worst case, thermal runaway may cause the cell to catch fire or to explode. The SEI degradation rate, also, increases with increasing temperature, and other cycling material is employed to

repair it as the SEI layer starts to break down. In addition, metastable organic SEI components are converted into inorganic products which are more stable on one hand, but on the other are less easily penetrable by solvent molecules, reducing the SEI conductivity for lithium [19].

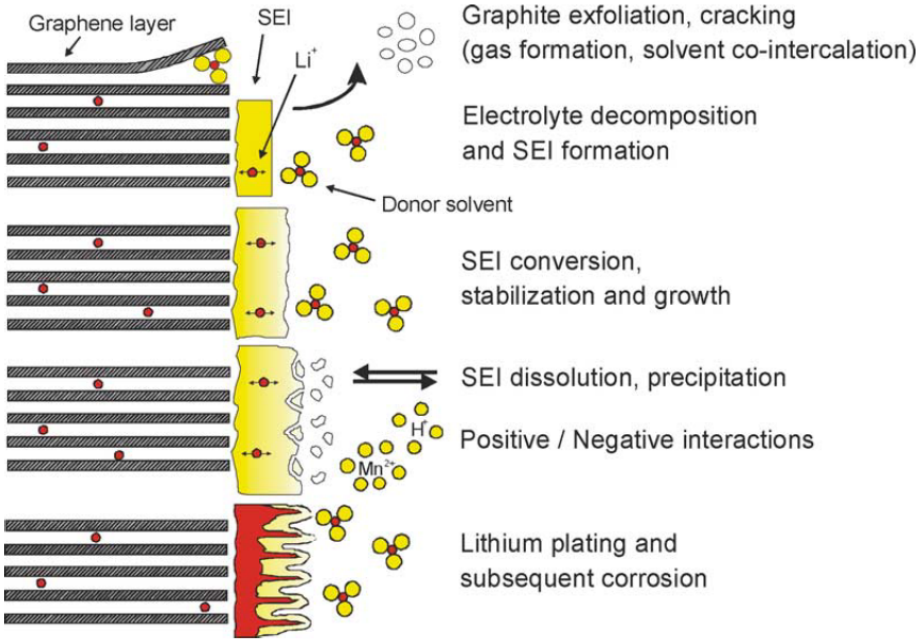

Figure 2.1: Changes at the anode/electrolyte interface

Low temperatures involve in different challenges. Since, the intercalation potential of carbonaceous anode materials, like graphite indeed, is close to the potential of lithium metal, at low temperature two effects are exhibited, metallic lithium plating and lithium dendrite growth. Subsequent reactions of the Li metal with the electrolyte induce, or at least accelerate, ageing and, furthermore, deteriorate safety [15].
It is clear that a stable SEI is basic to enlarge battery life and try to understand SEI formation mechanism and how its chemical composition evolves during aging would be already a step forward.

2.1.2 Ageing of NMC

Cathode materials affect significantly both performance data as well as cycling and calendar life of lithium-ion cells. NMC has been studied in the last years for usage in high energy and high power batteries. The mechanisms of capacity fading and their prevention are still of increasing interest and not completely understood at the moment. Some changes on the cathode may influence the life-time of a lithium-ion cell:

- ageing of active material;
- degradation or changes of electrode components like conducting agents, binder, corrosion of current collector;
- oxidation of electrolyte components and surface film formation;
- interaction of ageing products with the negative electrode.

These effects do not occur separately and can not be discussed independently from each other. They are very sensitive to individual electrode composition and are influenced by cycling and storage conditions [15]. In general, charge capacity fading of positive active material can originate from three basic principles:

- structural changes during cycling;
- chemical decomposition/dissolution reaction;
- surface film modification.

Fig. 2.2 summarizes the main causes of NMC ageing.

2.2 Experimental procedure

In this section, the procedure and tools used for characterizing aging in batteries are introduced.

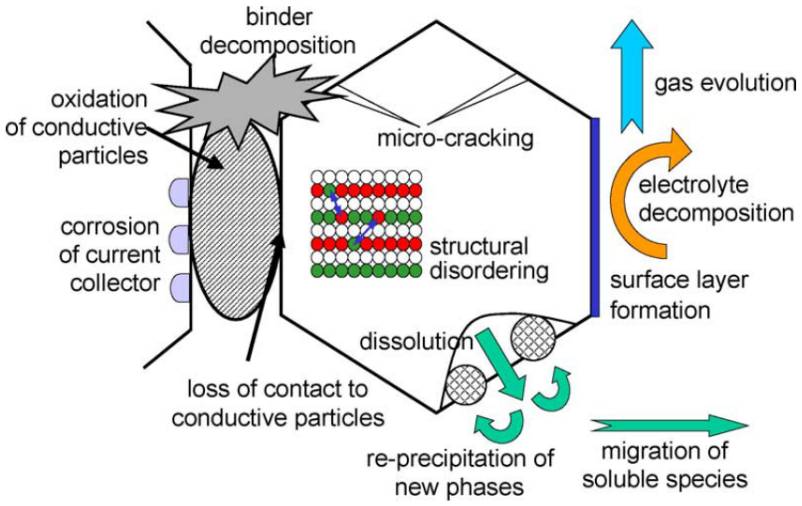

Figure 2.2: Overview of the main causes of NMC ageing

2.2.1 Reference characterization procedure

For both, calendar and cycle ageing, ageing mechanism are investigated alternating electrochemical characterizations at a reference condition with storage or cycling periods at predefined conditions. The aim of the reference characterization procedure is to collect data on ageing at different ageing states. The procedure comprises a capacity test, a micro rate test, a pulse test and, finally, an electrochemical impedance spectroscopy.
Experimental campaign on calendar aging require very long time tests, the cells are monitored for one or two years and are subjected to the reference characterization procedure every month [20]. The cells under study are subjected to the reference characterization procedure every 6 days due to limited time for this work.
Different reference characterization procedure are available in literature [20, 21, 22]. The procedure, for this purpose an *Arbin instrument* has been used, followed in this work consists of these steps:

- The cell is charged using CC charging up to E_{max} at a current rate of 1 C followed by CV charging until the current has decreased to 0.05 C (CCCV charging). Then it is kept at open circuit conditions for 30 min in order to let transient processes relax.

- Then, two cycles comprising of constant current discharging to E_{min} at 1 C and CCCV charging are carried out. The cell is held at open circuit conditions for 30 min after every charge and discharge.
- The cell is then CC discharged and CCCV charged at 0.1 C. The battery is held at open circuit conditions for 1 min after discharge and for 30 min after charge.The discharge capacity at C/10 $Q_{0.1C}$ is registered for the purpose of analysing capacity decrease over time.
- After, pulse tests are performed, in particular, a discharge pulse at a current rate of 2 C for 20 s and a charge pulse at a current rate of 2 C for 40 s. The resting period after the discharge pulse is 40 s and after the charge pulse is 5 min. The change in the SOC after one discharge and charge pulse is zero. The pulses applied at each 10 % SOC step between 100 % SOC and 0 % SOC. The SOC levels set by discharging 10 % of the capacity Q_{1C} at 1 C followed by a pause of 30 min.
- The cell is CCCV-charged with a current rate of 1 C. Then, 50 % of capacity Q_{1C} is discharged with a current rate of 1 C so that the cell is at 50 % SOC at the end of this step.
- For electrochemical impedance spectroscopy (EIS) the *Biologic Science Instrument* has been used. 8 points of measurement per decade are taken from 2.0 kHz down to 10 mHZ. The ideal voltage response is set to 10 mV and the maximum exciting current amplitude is set to 0.2 A.

2.2.2 Electrochemical impedance spectroscopy (EIS)

In this section a fundamental tool, electrochemical impedance spectroscopy (EIS), for the analysis reported hereafter, is presented. EIS is a non-invasive technique analyzing material properties and processes occurring at electrode/electrolyte interface. Additionally, it is a powerful method for evaluating the interface physic state and/or its ageing over time. The measurement approach typically consists of applying a sinusoidal current (galvanostatic mode, GEIS) or voltage (potentiostatic mode, PEIS) of a certain amplitude and frequency, and measuring the amplitude and phase shift of the output voltage or current, respectively. This procedure is repeated for a number of frequencies, typically in the kHz to mHz range, thereby

generating a characteristic impedance spectrum.
Thus if the input and output signals are:

$$\begin{cases} i(\omega,t) = |i|e^{j\omega t} \\ u(\omega,t) = |u|e^{j\omega t+\Phi} \end{cases} \tag{2.1}$$

where $|i|$ and $|u|$ are respectively AC current amplitude and AC voltage amplitude, ω is the frequency and Φ the phase angle.
The impedance is given by the ratio of voltage to current, and can be expressed as:

$$Z(\omega,t) = \frac{u(\omega,t)}{i(\omega,t)} = Re(Z) + j\dot{I}m(Z) = |Z|e^{j\Phi} \tag{2.2}$$

The impedance unit of measurement is [Ω] and it consists of a real part, called "resistor", and a imaginary part, "reactance", depending on frequency and material properties.

$$\begin{cases} Re(Z) = |Z|\cos\Phi \\ Im(Z) = |Z|\sin\Phi \end{cases} \tag{2.3}$$

The impedance is a transfer function, by definition the ratio between output signal and input signal, hence is suitable in cases in which a current is applied to the system as input and a voltage is the signal coming out. Otherwise, for the purpose, admittance is more appropriate, defined as Y=1/Z.
Features on the resulting Nyquist plot (where the imaginary part of the impedance is plotted against the real part) and/or Bode plot (where either magnitude and phase, or real and imaginary parts, are plotted as a function of frequency) enable parameterisation of the resistance, capacitance and inductance of the various cell components and processes. The inductive behaviour observed in the upper frequency range of the spectrum can be caused by cable of the measurement system. The high-frequency intercept with the real axis corresponds to the sum of internal ohmic resistances, like the electrolyte, active material, current collectors and electrical contacts. The semicircles in the mid-frequency range are due to the electrochemical processes occurring at the electrode/electrolyte interfaces inside the cell, which combine resistive and capacitive effects. At each electrode, lithium transport through the SEI occurs in parallel with dielectric polarisation, and lithium (de-)intercalation occurs in parallel with double layer (dis)charging. Thus there are

contributions from at least four different processes. The low-frequency tail, instead, reflects solid state lithium ion diffusion in the active material of the cell electrodes.

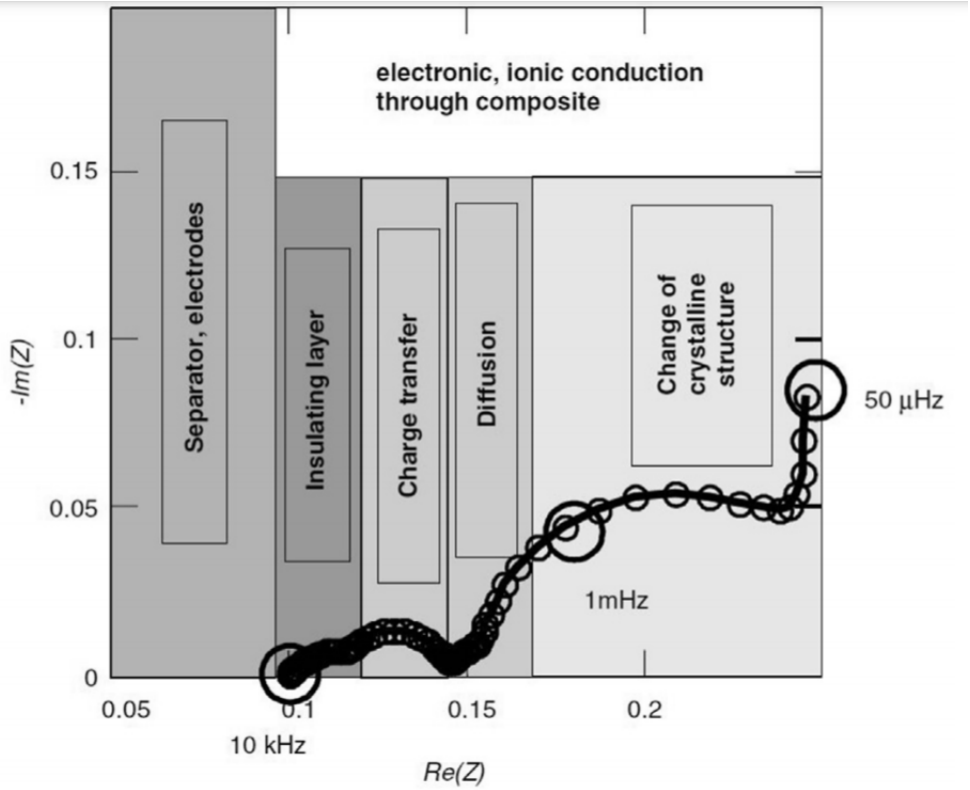

Figure 2.3: Graphical representation of a Li-ion cell EIS

2.2.3 Equivalent circuit model

Complex systems, as often happens, can be modelled by circuit. The basic approach is equivalent circuit model, which consists of electrical circuit elements in series or in parallel. The most common elements are resistors (R), capacitors (C) and inductors (L).

- Resistor describes dissipative phenomena and its unit of measurement is [Ω]. The equation describing this impedance type is Eq. 2.4. On the Nyquist plot this impedance is a point on the real axis.

$$Z_R(\omega) = R \tag{2.4}$$

- Capacitors give information about electric charge storage in an electric field and dielectric polarisation. The impedance gets only imaginary part, Eq. 2.5, in Farad [F = Ω^{-1} s] and on Nyquist plot is a vertical line growing if frequency increases.

$$Z_C(\omega) = -\frac{j}{\omega C} \tag{2.5}$$

- Inductors describe electric storage in a magnetic field when electric current flows through it. As capacitors, the impedance gets only imaginary part in Henry [H = Ω s]. On Nyquist plot is a vertical line decreasing if frequency increases.

$$Z_L(\omega) = j\omega L \tag{2.6}$$

Other two components, constant phase element (CPE) and Warburg element, describes non homogeneous electrochemical systems, whose phenomena depend on frequency.

- The CPE is defined by two values, the generalized capacitance K [Ω^{-1} s^n] and the depression factor n, the phase angle related to n is n $\cdot$ $\pi/2$. If n equals 1, the equation Eq. 2.7 is identical to that of a capacitor. If n equals to 0.5, a 45° line is produced on the complex plane graph. When a CPE is placed in parallel to a resistor, a ZARC element (depressed semi-circle) is produced. The constant phase element is used in a model in place of a capacitor to compensate for non homogeneity in the system. For example, a rough or porous surface can cause a double layer capacitance to appear as a constant phase element with a n value between 0.9 and 1. In fact, a capacitor is actually a constant phase element with a constant phase angle of 90°.

$$Z_{CPE}(\omega) = \frac{1}{K\sqrt[n]{j\omega}} \tag{2.7}$$

- A Warburg element occurs when charge carrier diffuses through a material. Lower frequencies correspond to diffusion deeper into the material. If the material is thin, low frequencies will penetrate the entire thickness, creating a Finite Length Warburg element. If the material is thick enough so that the lowest frequencies applied do not fully penetrate the layer, it must be

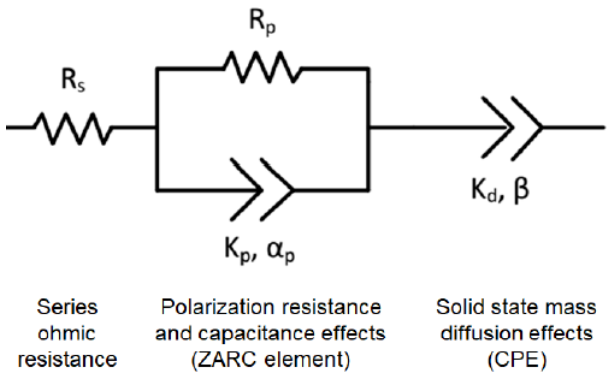

Figure 2.4: Calendar aging model

interpreted as infinite. The unit of measurement is [Ω^{-1} $s^{0.5}$] and the equation describing the Warburg element is Eq. 2.8.

$$Z_W(\omega) = \frac{W}{\sqrt{j\omega}} = \frac{W}{\sqrt{\omega}} \cdot (1 - j) \tag{2.8}$$

The circuit model (Fig. 2.4) has been thought to represent the cell processes, related to calendar aging, as a series parallel combination of the above mentioned elements. *ZView* software has been used for fitting impedance data and determining the parameters of the circuit model. To avoid over fitting, only the dominant processes happening inside the cells are considered during fitting.

For the cells under study, inductive effects are not observed at frequencies between 2.0 kHz and 10 mHz, therefore the inductor is not put in the model. The intersection of the curve with the real axis represents mainly ohmic resistance of the electrolyte (R_s). The dominant processes in the electrode is represented by ZARC element which is a combination of a constant phase element (CPE) with resistance in parallel. Representation of the electrode processes using a ZARC element is accurate as long as the diffusion tail is separated from the charge transfer loop [23]. A new cell is expected to have a small SEI resistance and thus the semicircle seen in the spectrum will be due to the charge transfer resistance of the two electrodes. Hence, in the calendar aged cells, the cell spectra consisted of mostly only one depressed semicircle. For this reason, only one ZARC element is used for representing processes for both electrodes. Solid state diffusion process is manifested as a sloped line in the spectra [23]. Usually, Warburg element is used

to represent diffusion processes, but this is only valid when the slope of diffusion tail is about 45°, highlighting a semi-infinite diffusion [21]. The slopes for the cells tested in this work are greater than 45°, therefore a CPE element represents better the trend.
The cell impedance for this equivalent circuit is:

$$Z(\omega) = R_s + \frac{R_p}{1 + (j\omega\tau)^{\alpha_p}} + \frac{1}{K_d(j\omega)^{\beta}} \tag{2.9}$$

2.3 Calendar ageing tests

In this section the results of calendar aging studies on coin cells 2032 are reported, focusing on changes of both cell capacity and cell impedance. For the latter, variation of equivalent circuit parameters are taken in account, linking them with degradation phenomena occurring inside batteries.
The characterization procedure and the storage duration are not standardized, changing type of li-ion batteries and their applications. The storage duration varies from 20 days [24], to 30 [20], to 60 [25]. In this work, due to lack of time, the batteries have been characterized every 6 days. The results shown are referred to 1 month of observed aging, under ambient temperature. EV's applications require a minimum battery capacity loss over more than 10 years, and since it would be a such extensive test period, usually accelerating aging tests are performed, the cells are stored at high temperature in order to accelerate degradation. The calendar aging dependence on temperature has not been tested, but would be interesting to study in which way the temperature increase or/and decrease it would affect impedance parameters and capacity fade. In this study, only the dependence on SOC will be discussed. In particular, after the EIS measurements, performed at 50 % SOC, the cells have been set to a precise state of charge, the cells tested at 50 % SOC, have not needed to a SOC resetting, instead the 100 % SOC, at 1C up to maximum voltage.
In order to see statistical effects, each test has been performed with two cells. In addition, four cells are used as reference batteries for the purpose of evaluating the influence of characterization procedure on capacity fade.

The same procedure has been done both for graphite/NMC622 batteries and lithium/NMC622 batteries, thus 16 cells have been assembled in total.

	n° of cells	
SOC	50 %	100 %
Reference cells	2	2
Cell characterized every 6 days	2	2

Table 2.1: Number of cells tested and their combination

2.4 Calendar ageing results and discussion

In this section the results obtained from the study will be reported and discussed. First of all, the initial capacity of graphite/NMC622 coin cells is constant enough, its mean value is 4.89 mAh, with a deviation of about +/- 0.2 mAh. Instead, the initial capacity of lithium/NMC622, as evidence of what said before, is higher, its mean value is 5.56 mAh with a deviation of only +/- 0.1 mAh.

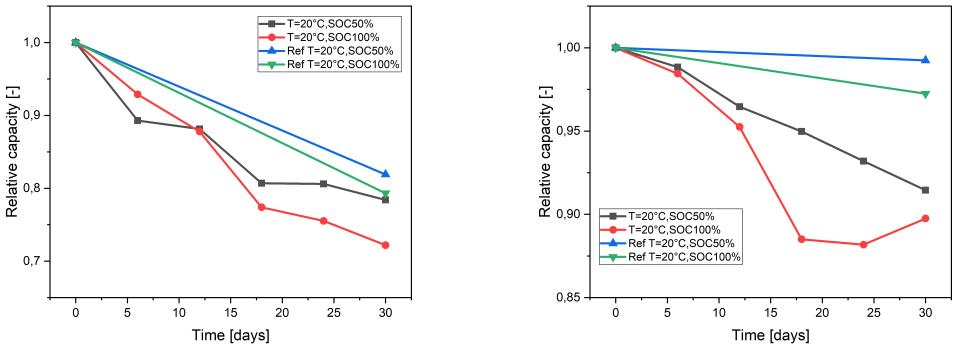

(a) Graphite/NMC622 relative capacity (b) Lithium/NMC622 relative capacity

Figure 2.5: Relative capacity trend

The major sources of calendar aging are irreversible side-reactions occurring especially at negative electrode, causing a cyclable lithium drop, loss of electrode active material due to particle insulation or other degradation mechanisms [26]. Thus, the main causes of capacity fade are ascribed to chemical reactions rather than electrochemical ones. The graphs highlight the calendar aging dependence on SOC. For both, cells stored at SOC 100 % show a capacity degradation more noticeable than cells stored at SOC 50 %. Keil at all. [27] study reveals a strong dependence of aging on lithiation level of graphite electrode, so a SOC higher than

50 % provides a capacity fade acceleration during storage period. The cause is probably the low anode potential which promotes loss of cyclable lithium, speeding up electrolyte reduction and SEI growth [20]. Moreover, an important factor to keep in mind is that graphite electrode is recycled from 500 BEV, thus the degradation is more relevant than lithium/NMC622 cells. Lithium metal anode gets a potential lower than graphite but that one used for assembling coin cells is fresh lithium, as well.
The cells, that have been characterized only at the beginning and after 30 days, show a capacity fade clearly lower than others, that is the proof that characterization procedure affects aging. This difference is more evident for lithium/NMC622 cells, probably for the same reasons before explained. This general trend will be seen also for equivalent circuit parameters R_s, R_p, α_p and τ_p.

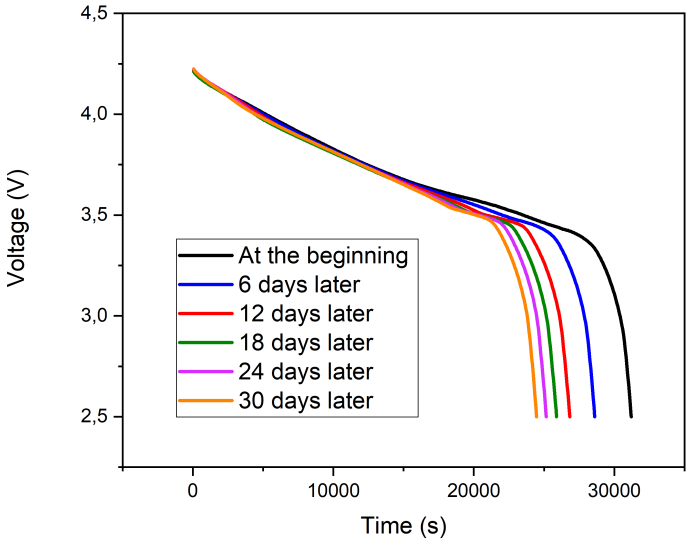

Figure 2.6: Graphite/NMC622 discharge curve at C/10

Fig. 2.6 and Fig. 2.7 display discharge curve at a current rate of C/10 of a graphite/NMC622 coin cell and a lithium/NMC622, respectively. The discharge curves have a gradual drift towards left over time, underlining the loss of capacity occurring.

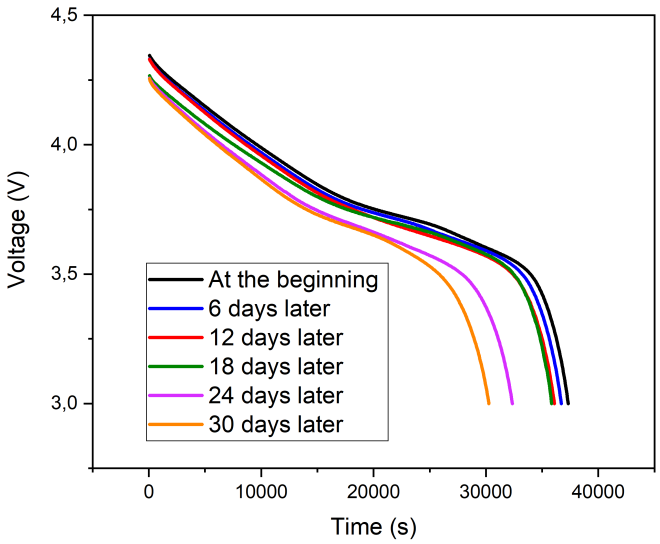

Figure 2.7: Lithium/NMC622 discharge curve at C/10

2.4.1 Series resistance

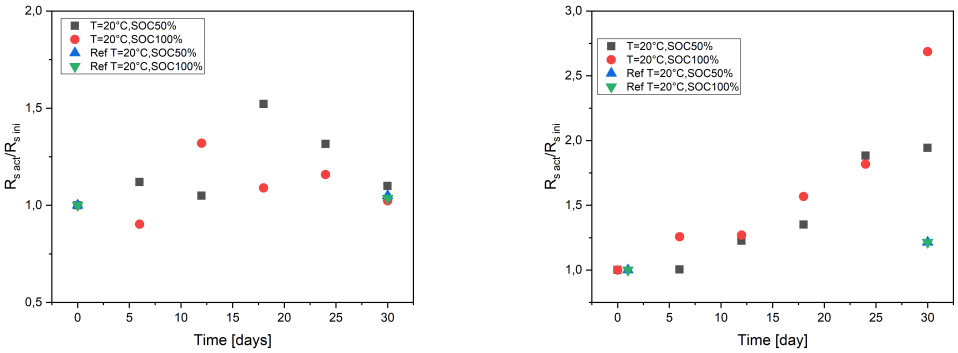

(a) Graphite/NMC622 (b) Lithium/NMC622

Figure 2.8: Relative series resistance

The series resistance points to ohmic resistance in the cell, in particular caused by a worsening in lithium conduction of electrolyte, due to its irreversible reactions with cyclable lithium. Fig. 2.8 shows a upward trend over time. This aspect is

clear especially for lithium/NMC622, Fig. 2.11(a) does not show an evident trend, both by the few available data number and the low quality materials. Probably, enlarging the storage duration an evident tendency will arise.
In addition, cells stored at 100 % SOC gets growth rate higher than cells stored at lower SOC, even if this pattern is not obvious in figures reported.

2.4.2 Parallel resistance

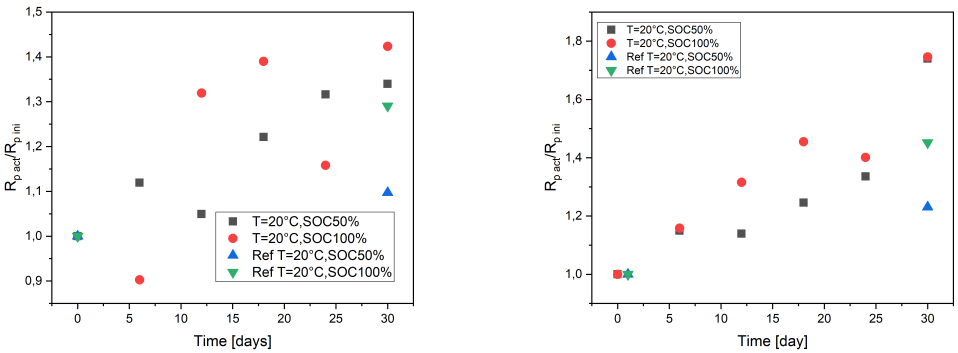

(a) Graphite/NMC622 (b) Lithium/NMC622

Figure 2.9: Relative parallel resistance

Polarization resistance trend sees a connection with chemical composition variation, growth of SEI layer, loss of active material of the positive electrode or a change of crystal structure. R_p may be basically seen as a combination of two contributions, resistance of SEI layer as well as charge transfer resistance across positive electrode. These two influences could change with a different rate and this is probably the explanation for irregular nature of parallel resistance. Surely, the main contribution is due to R_{SEI}; the upward trend of series resistance draws the attention to side reactions, SEI formation, happening at negative electrode, leading to an electrolyte decomposition. Furthermore, an higher voltage storage, as said, leads to an increase of electrolyte breakdown and, hence, a strong dependence on SOC.

2.4.3 Depression factor

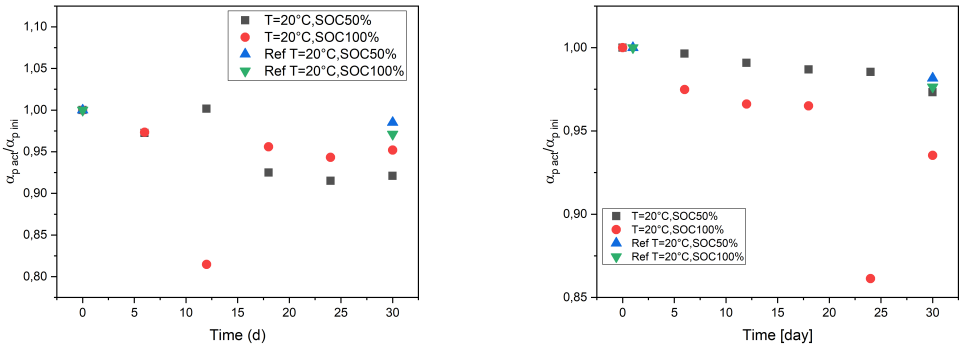

(a) Graphite/NMC622 (b) Lithium/NMC622

Figure 2.10: Depression factor trend

Depression factor, α_p, gives a measure of electrode uniformity, and thus of its porosity over time [28]. The depression of the semicircles given by ZARC element on Nyquist plot provides its numerical value. Depression factor drop is noticed in Fig. 2.10, sign of an increase of electrode non-uniformity, and probably of electrode porosity, as well. Particle fragmentation could be a cause of higher porosity and leads to a resistance growth [29]. So, an increase of semicircle depression points out a rise of electrodes roughness and a reduction of depression factor values. Moreover, Fig. 2.10 shows lower depression factor values at higher SOC, likely due to more irreversible reactions occurring at higher voltage which could produce particle fragmentation and a more porous material.

2.4.4 Mean time constant

The mean time constant is an ageing parameter which measures the dynamic behaviour of the cell [30]. Hence, a greater value of τ_p suggests a slower response of the battery to a current pulse. This growth is evident, Fig. 2.11, for both type of batteries, especially, again, for 100 % SOC.

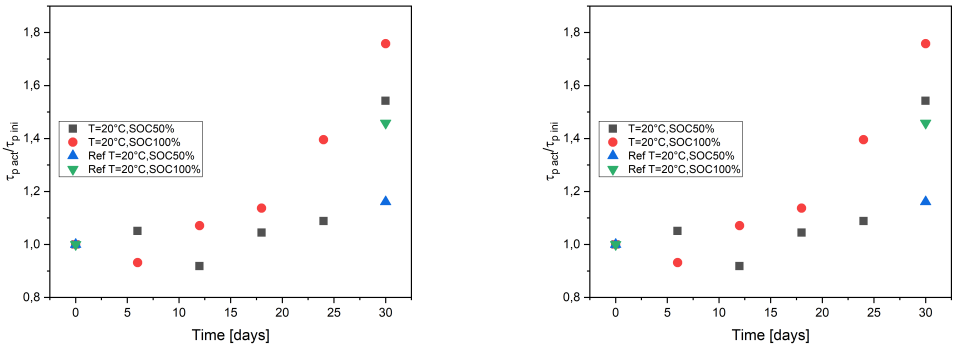

(a) Graphite/NMC622 (b) Lithium/NMC622

Figure 2.11: Mean time constant trend

2.5 Cycle ageing

Most vehicles are in park mode 95 % of the time during their life. But, studying the loss of performance by degradation processes occurring over their operation is interesting, as well. Usually, cycle ageing is studied changing different conditions, such as temperature, state of charge, depth of discharge (DOD) and current amplitude, in order to estimate the dependence on these parameters. At higher DOD, it means that the cells are almost fully charged and discharged up to very low SOC, higher temperature and at higher current rate, a higher capacity fade is seen.

As done for calendar ageing, cycling periods have been alternated with reference characterization procedures. In this document, only 4 cells have been assembled employing lithium as negative electrode, considering higher performance compared to graphite. The operating conditions are summarized in the table below

	n° of cells
DOD100	
C/2 D1	2
C1 D2	2

Table 2.2: Total cells assembled

DOD100 means that cells are charged and discharged from SOC 0 % to SOC

100 % and vice versa, C/2 D1 means that the cells are charged at a current rate of C/2 and discharged at 1C, hence C1 D1 means that the cells have worked at 1C. Unfortunately, two cells, one at C/2 D1 condition and one at C1 D2, have given awful results already during initial characterization procedure, for this reason results are not reported. The others have finished well the procedure and then have been cycled until 100 equivalent full cycle (EFC) have been reached. For both of them, the capacity trend cycle by cycle is shown in Fig. 2.12 and Fig. 2.13. The initial capacity is a little bit lower than 5.56 mAh because a certain amount is lost during characterization procedure. From the figures it is possible to notice a fast capacity decline after few cycles, especially for a higher charging current rate. Cells charged at 1 C shows a capacity fade of about 2.5 mAh after only 10 EFC. Thus, cycle ageing is strongly dependent on current rate, an higher ionic current density demands faster reactions and diffusion, which arouse mechanical stresses, anode cracks, and as a consequence other cyclable lithium employed to repair SEI, and a faster degradation [31].
In light of the results obtained any other coin cell have not been assembled for studying cycle ageing.

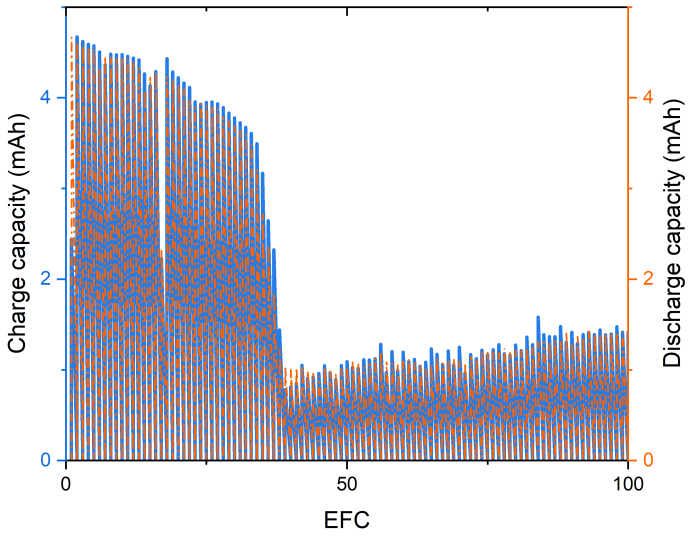

Figure 2.12: DOD100 C/2 D1

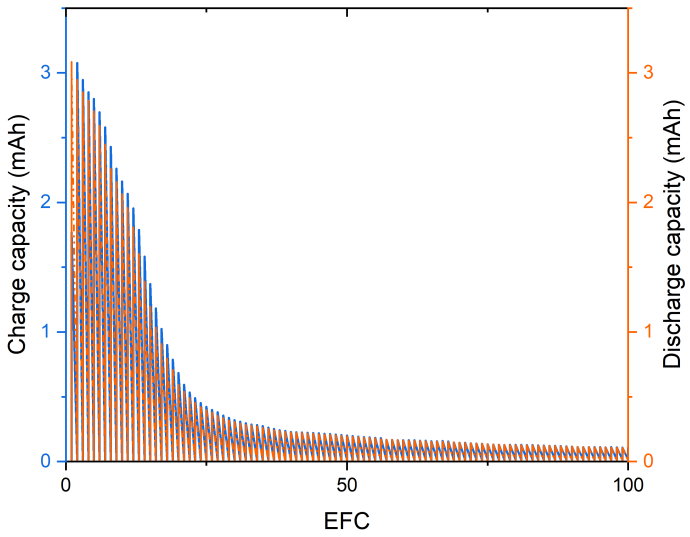

Figure 2.13: DOD100 C1 D2

Part II

Modelling

Chapter 3

Electrochemical-thermal modelling

The aims of modelling lithium-ion batteries are to gain insights to cells internal phenomena, forecast their operation and optimize cell design parameters. Various type of mathematical models have been developed. The simplest one and computationally faster is battery management system (BMS), it performs a number of critical duties including protecting the battery from misuse, matching power demands, providing optimal charging profiles and managing cell balancing among others [32].

The next two levels of modelling, more complex compared to BMS and computationally expensive, are single particle model (SPM) and pseudo two dimensional (P2D) model. The SPM is a simple model that deems each electrode as a single particle and looks into transport processes in the solid phase, but leaves out concentration and potential effects between particles in the solution phase [33]. The P2D model has a more detailed approach, it takes in account several physically significant internal variables such as potentials within electrolyte and solid phase and Li^+ concentration in both phases. Nonlinear Butler-Volmer kinetics are employed to model electrochemical system and, additionally, starting from P2D model other phenomena can be easily added like thermal management or capacity fade. All these features make P2D a very useful tool, but it has also several drawbacks. The most important one is its high computational cost, due to the high set of differential equations, that represent mass balances, charge balances, electrochemical reaction

kinetics and thermal energy balance, which have to be solved. Finally, kinetic Monte Carlo (KMC) method is the most complex model and can help to predict thermodynamic properties of materials or mobility of lithium inside the crystal structure.

3.1 The electrochemical model

The goal in this chapter is to develop an electrochemical model for forecasting the behaviour of high energy density lithium-ion battery. The best approach, for this purpose, is that of developing a P2D model [34]. The most interesting aspect of this kind of model is the possibility of putting micro and macro scale phenomena together. As may be seen in Fig. 3.1 porous electrodes consist of active material particles surrounded by a liquid phase, electrolyte. Micro scale process refers to diffusion through active material surface. Instead, macro scale phenomena are related to transfer processes, predominantly unidirectional, along battery thickness; hence, a 1D mathematical model (x-axis) may be applied. These two domains are connected by law of conservation of species.

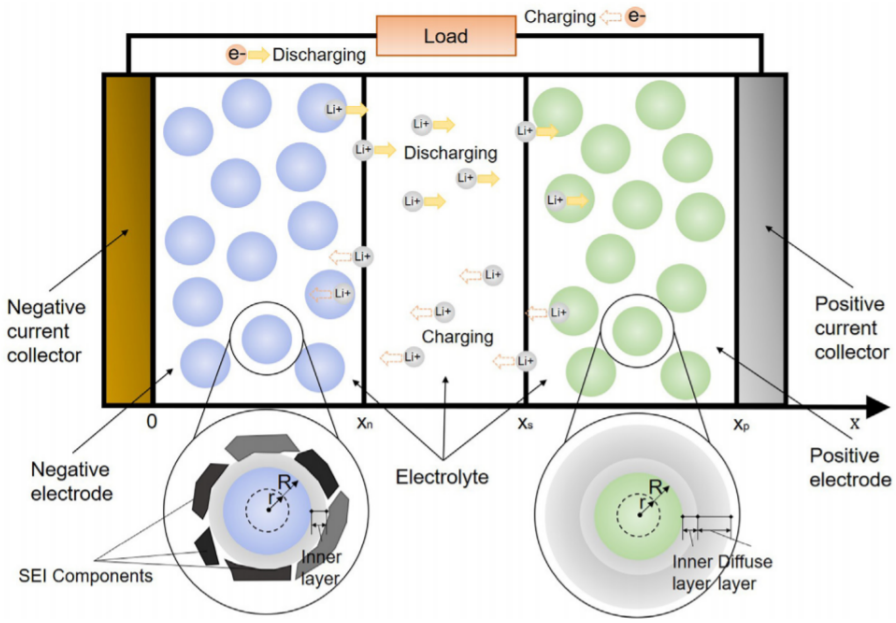

Figure 3.1: Schematic of li-ion battery

During discharge, Li^+ diffuses to negative active material particles surface, here reacts and then moves to electrolyte phase. By migration and diffusion, convection is neglected in this model, Li ions are transported through electrolyte towards inner surface of positive active particles. According Fick's laws of diffusion, the Li^+ concentration into solid phase is described as

$$\frac{\partial c_s}{\partial t} = \nabla \cdot (-D_{s,eff} \cdot \nabla c_s) \tag{3.1}$$

where
$D_{s,eff}$ is the effective Li^+ diffusion coefficient in the solid particle ($m^2\ s^{-1}$)
with boundary and initial conditions

$$\frac{\partial c_s}{\partial r}\Big|_{r=0} = 0 \tag{3.2}$$

$$-D_{s,eff} \cdot \frac{\partial c_s}{\partial r}\Big|_{r=r_p} = -\frac{J_{Li}}{a_v \cdot F} \tag{3.3}$$

$$c_s(x, r, 0) = c_{s,0} \tag{3.4}$$

where
J_{Li} is the current density flux of charges in solid phase ($A\ m^{-3}$)
F is the Faraday constant equals to 96485 ($C\ mol^{-1}$)
a_v is the specific inter-facial area (m^{-1})
Li^+ concentration changes in the electrolyte occur due to three processes: diffusion, related to concentration gradient, migration, caused by potential gradient and convection, because of pressure differences. The solvent velocity is not substantial in lithium-ion battery, as a matter of fact convection processes are negligible [35]. Therefore, a mass balance in the electrolyte gives

$$\epsilon_l \cdot \frac{\partial c_l}{\partial t} = \nabla \cdot (D_{l,eff} \cdot \nabla c_l) - \nabla \cdot (\frac{i_l \cdot t_+}{F}) + \frac{\nabla \cdot J_l}{F} \tag{3.5}$$

where
ϵ_l is the volume fraction of the solution phase
$D_{l,eff}$ is the effective Li^+ diffusion coefficient in the electrolyte
t_+ is the transference number

Transference n° t_+ considers the fraction of the total ionic conductivity carried by cations only [36].
The boundary and initial conditions are

$$\frac{\partial c_l}{\partial x}\Big|_{x=0} = \frac{\partial c_l}{\partial x}\Big|_{x=L} = 0 \tag{3.6}$$

$$c_l(x,0) = c_{l,0} \tag{3.7}$$

Effective ionic diffusion coefficients into solid and liquid phase are related to porosity of porous media and tortuosity, both of them affect Li^+ transport.

$$\tau = \epsilon^{1-\beta}, \quad D_{eff} = D_{ref} \cdot \epsilon^{\beta} \tag{3.8}$$

where β is the Bruggeman coefficient with the value of 1.5 for a porous medium composed of mono-disperse, non-porous isotropic spherical particles small compared to the thickness of the porous medium [37].
Along with this, ohm's law describes charge conservation in the solid phase

$$i_s = -\sigma_{s,eff} \cdot \nabla \cdot \Phi_s \tag{3.9}$$

$$\sigma_{s,eff} = -\epsilon_s^{1.5} \cdot \sigma_s \tag{3.10}$$

where
i_s is the current density in the solid (A m^{-2})
$\sigma_{s,eff}$ is the effective electrical conductivity in the solid (S m^{-1})
σ_s is the conductivity in the solid phase (S m^{-1})
Φ_s is the potential at the solid surface (V)
Eq. 3.11 makes boundary conditions at current collectors explicit, being proportional to applied current density.

$$-\sigma_{s,eff} \cdot \frac{\partial \Phi_s}{\partial x}\Big|_{x=0} = -\sigma_{s,eff} \cdot \frac{\partial \Phi_s}{\partial x}\Big|_{x=L} = i_{app} \tag{3.11}$$

$$-\sigma_{s,eff} \cdot \frac{\partial \Phi_s}{\partial x}\Big|_{x=L_p} = -\sigma_{s,eff} \cdot \frac{\partial \Phi_s}{\partial x}\Big|_{x=L_p+L_s} = 0 \tag{3.12}$$

where L_p and L_s are, respectively, positive electrode and separator thickness.
Charge conservation in electrolyte phase is explained combining Kirchoff's law with Ohm's law

$$i_l = -\sigma_{l,eff} \cdot \nabla \cdot \Phi_l + \frac{2 \cdot R \cdot T \cdot \sigma_{l,eff}}{F} \cdot (1 - t_+) \cdot (1 + \frac{\partial \ln f}{\partial \ln c_l}) \cdot \nabla \cdot \ln c_l \quad (3.13)$$

$$\sigma_{l,eff} = -\epsilon_l^{1.5} \cdot \sigma_l \quad (3.14)$$

where
i_l is the current density in the liquid phase (A m^{-2})
$\sigma_{l,eff}$ is the effective electrical conductivity in the electrolyte (S m^{-1})
σ_l is the conductivity in the liquid phase (S m^{-1})
Φ_l is the potential in the solution (V)
R is the gas constant equals to 8.314 (J K^{-1} mol^{-1})
T is the temperature (K)
F is the Faraday constant equals to 96485 (C mol^{-1})
f is the mean molar activity
The boundary condition is

$$\left.\frac{\partial \Phi_l}{\partial x}\right|_{x=0} = \left.\frac{\partial \Phi_l}{\partial x}\right|_{x=L} = 0 \quad (3.15)$$

Looking at interface between solid and electrolyte phase, kinetics of insertion and extraction of Li^+ are described by Butler-Volmer equations. In particular, Eqs. 3.16 and 3.17 make clear the rate of reaction occurring at the interface between these two phases.
In liquid phase

$$J_{Li,l} = \nabla \cdot i_l = a_v \cdot i_0 \cdot [\exp(\frac{\alpha_a \cdot F \cdot \eta}{R \cdot T}) - \exp(\frac{-\alpha_c \cdot F \cdot \eta}{R \cdot T})] \quad (3.16)$$

In solid state

$$J_{Li,s} = \nabla \cdot i_s = a_v \cdot i_0 \cdot [\exp(\frac{\alpha_a \cdot F \cdot \eta}{R \cdot T}) - \exp(\frac{-\alpha_c \cdot F \cdot \eta}{R \cdot T})] \quad (3.17)$$

where
i_0 is the exchange current density (A m^{-2})

a_v is the specific inter-facial area (m^{-1})
α is the charge transfer coefficient; subscripts a and c refer, respectively, to anode and cathode
η is the surface over-potential (V)
The specific inter-facial area of each electrode depends on the spherical particle radius (r_p) of porous electrode and the volume fraction of the solid active material (ϵ_s). The relationship is clarified in the Eq. 3.18.

$$a_v = \frac{3 \cdot \epsilon_s}{r_p} \tag{3.18}$$

The exchange current density is defined as

$$i_0 = F \cdot k_c^{\alpha_a} \cdot k_a^{\alpha_c} \cdot (c_{s,max} - c_s)^{\alpha_a} \cdot c_s^{\alpha_c} \cdot (\frac{c_l}{c_{l,ref}})^{\alpha_a} \tag{3.19}$$

where
k is the rate constant of the electrochemical reaction (m s^{-1})
$c_{s,max}$ is the maximum concentration of lithium in the solid phase (mol m^{-3})
c_s is the instantaneous concentration of lithium in the solid phase (mol m^{-3})
c_l is the instantaneous concentration of lithium in the liquid phase (mol m^{-3})
$c_{l,ref}$ is the reference concentration of lithium in the liquid phase (mol m^{-3})
The exchange current density is the current at zero over-potential, for a redox reaction at the equilibrium the electrons migrate between electrodes and electrolyte, in both direction. Thus, if the potential is set more negative, the anodic current will be higher than cathodic current. This dependence is made explicit through transfer coefficients, α_c and α_a. Exchange current density depends also on the lattice sites in the electrode material left empty, ($c_{s,max}$-c_s). When the concentration in the solid phase equals its maximum value or is zero, the exchange current density is null.
Hence, the over-potential is the additional potential producing an increase in thermodynamic driving force for the processes. It is defined as

$$\eta = \Phi_s - \Phi_l - E_{eq} - R_{film} \cdot i \tag{3.20}$$

where
E_{eq} is the equilibrium potential of the electrode material (V)
R_{film} is the film resistance due to SEI layer (Ω m^2)

i is the sum of intercalation/deintercalation current density and current density caused by parasitic reaction taking place at the anode/electrolyte interface (A m^{-2}) [38]

3.2 A model for predicting capacity fade due to SEI layer formation with negative graphite electrode

A lithium-ion battery feature is degradation occurring over time. Electrolyte decomposition, loss of active material and loss of cycleable lithium are some aging phenomena contributing to time degradation [15].
For cells employing graphite as negative electrode, cycleable lithium is lost mostly due to SEI layer formation on graphite surface. The SEI film is rough in morphology and non-uniform in composition, including small splits on the surface [39].
The model developed in this work focuses on film formation at C-rates equal to or lower than 1C, where the main degradation cause is loss of active lithium for forming or repairing SEI layer at this current range [40]. The expression describing SEI forming reaction is a cathodic Tafel form, combined with a limiting current due to diffusion through the SEI, using first order electrolyte solvent decomposition kinetics and linear solvent diffusion [41]. The model considers that reacting species pass through SEI micro and macro pores being created over time, as can be seen in Fig 3.2. If micro pores are always present, macro pores are created by graphite particle expansion during charge. Thus, the total SEI layer current formation is the combination of two linear contributions. The former is the SEI current on the region where the film is intact, the second one is that on the region where macro pores are formed due to graphite particles expansion. Therefore, i_{SEI} may be expressed as

$$i_{SEI} = i_{cov} + i_{crd} \tag{3.21}$$

where
i_{cov} is the current contribution related to graphite particles covered by an intact and micro pores SEI layer (A m^{-2})

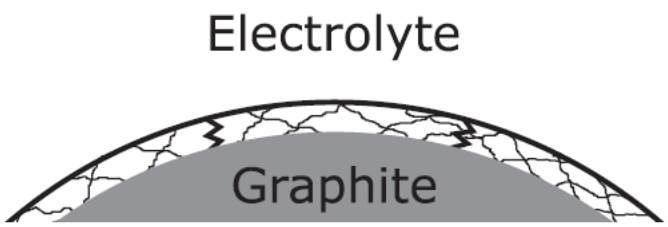

Figure 3.2: Cracks formed in the micro porous SEI layer due to expansion of the graphite particle

i_{crd} is the current contribution related to graphite particles covered by a split SEI layer (A m^{-2})

As said above, the SEI forming current can be described as a cathodic Tafel expression, so the current for the covered areas is

$$i_{kin,cov} = -\epsilon_{cov} \cdot i_0 \cdot \exp -\frac{\alpha \cdot \eta_{SEI} \cdot F}{R \cdot T} \tag{3.22}$$

where
i_0 is the exchange current (A m^{-2})
ϵ_{cov} is the porosity of the micro porous part of the SEI layer
α is the cathodic transfer coefficient
η_{SEI} is the over potential of the SEI forming reaction (V)
The over potential of the SEI is defined as

$$\eta_{SEI} = \Phi_s - \Phi_l - E_{eq,SEI} \tag{3.23}$$

The current on parts where SEI layer is cracked gets the same form of i_{cov}

$$i_{kin,crd} = -\epsilon_{crd} \cdot i_0 \cdot \exp -\frac{\alpha \cdot \eta_{SEI} \cdot F}{R \cdot T} \tag{3.24}$$

where ϵ_{crd} is the volume fraction of the cracks in the SEI layer. For evaluating ϵ_{crd} a dependence on the graphite expansion rate is assumed

$$\epsilon_{crd} = a_{crd} \cdot K_{crd} \tag{3.25}$$

where
a_{crd} is a proportionality factor

K_{crd} is the graphite expansion function
K_{crd} is a piece-wise function and depends in turn on intercalation current and SOC [42].

$$\begin{aligned} K_{crd} &= -2 \cdot \frac{I_{ical}}{I_{1C}} \quad I_{ical} < 0 \; and \; SOC < 0.3 \\ K_{crd} &= 0 \quad I_{ical} < 0 \; and \; 0.3 \leq SOC \leq 0.7 \\ K_{crd} &= -2 \cdot \frac{I_{ical}}{I_{1C}} \quad I_{ical} < 0 \; and \; SOC > 0.7 \\ K_{crd} &= 0 \quad I_{ical} \geq 0 \end{aligned} \tag{3.26}$$

Instead, the limiting current is assumed to be inversely proportional to SEI layer thickness s, the two contributions are defined as follow

$$i_{lim,cov} = -\frac{\epsilon_{cov} \cdot c \cdot D_{cov} \cdot F \cdot A}{s} \tag{3.27}$$

$$i_{lim,crd} = -\frac{\epsilon_{crd} \cdot c \cdot D_{crd} \cdot F \cdot A}{s} \tag{3.28}$$

where
c is the bulk concentration of SEI forming reactant in the electrolyte
D_{cov} and D_{crd} is the diffusion coefficient respectively in the covering layer and in the cracked layer
The two diffusion coefficients are associated to tortuosity of macro and micro pores

$$D_i = \frac{D}{\tau_i} \tag{3.29}$$

where D is the diffusion coefficient of reacting species in the electrolyte.
Now, defining a dimensionless relative expansion factor for the cracked parts H

$$H = \frac{a_{crd}}{\epsilon_{cov}} \tag{3.30}$$

it is possible to put in relationship the two current contributions

$$i_{crd} = H \cdot K_{crd} \cdot i_{cov} \tag{3.31}$$

The SEI current on micro porous film layer is obtained putting in relationship limiting and kinetic current in this way

$$i_i = \frac{i_{kin,i}}{1 + \frac{i_{kin,i}}{i_{lim,i}}} \tag{3.32}$$

Thus,

$$i_{cov} = -\frac{J \cdot i_{1C}}{\exp(\frac{\alpha \cdot \eta_{SEI} \cdot F}{R \cdot T}) + \frac{q_{SEI} \cdot f \cdot J}{i_{1C}}} \tag{3.33}$$

where J and f are two lumped parameters derived from the model. J is dimensionless and evaluates as

$$J = \frac{\epsilon_{cov} \cdot i_0}{i_{1C}} \tag{3.34}$$

f is a frequency parameter (1/s)

$$f = \frac{\tau_{cov} \cdot V \cdot i_{1C}^2}{\epsilon_{cov} \cdot (1 - \epsilon_{cov}) \cdot c \cdot D \cdot F \cdot A^2} \tag{3.35}$$

Therefore, the SEI current on cracked layer is

$$i_{crd} = -H \cdot K_{crd} \cdot \frac{J \cdot i_{1C}}{\exp(\frac{\alpha \cdot \eta_{SEI} \cdot F}{R \cdot T}) + \frac{q_{SEI} \cdot f \cdot J}{i_{1C}}} \tag{3.36}$$

so that, the total density current on the particle surface is

$$i_{SEI} = -(1 + H \cdot K_{crd}) \frac{J \cdot i_{1C}}{\exp(\frac{\alpha \cdot \eta_{SEI} \cdot F}{R \cdot T}) + \frac{q_{SEI} \cdot f \cdot J}{i_{1C}}} \tag{3.37}$$

q_{SEI} depends on SEI concentration according to

$$q_{SEI} = \frac{F \cdot c_{SEI}}{A_v} \tag{3.38}$$

where

A_v is the electrode surface area (m^{-1})

The change in SEI concentration is expressed by differential form of Faraday's law

$$\frac{\partial c_{SEI}}{\partial t} = -\frac{\upsilon_{SEI} \cdot i_{SEI}}{n \cdot F} \tag{3.39}$$

Thus, knowing SEI concentration the thickness of the film can be calculated

$$\delta_{film} = \delta_{film,0} + \frac{c_{SEI} \cdot M_P}{A_v \cdot \rho_P} \tag{3.40}$$

where
M_p is the molar weight of product formed by side reaction (kg mol^{-1})
ρ_p is the density of product formed by side reaction (kg m^{-3})
Finally, after evaluating the film thickness getting greater and greater over time, the film resistance is found

$$R_{film} = \frac{\delta_{film}}{\kappa_{SEI}} \tag{3.41}$$

where κ_{SEI} is SEI layer conductivity (S m^{-1})

3.3 Thermal modeling

Exothermic reactions occurring inside cell can generate a system over heating and produce a reactions acceleration between cell components, especially if the heat transfer towards external environment is not so efficient [43]. Therefore, a particular attention is directed to how thermal management and temperature influence thermal runaways, capacity and power fade and packaging. Bandhauer et all summarise the main thermal issues in this kind of systems [44]. For designing a safe cell, it is suitable to include heat generation processes and variable dependence on temperature in the electrochemical model illustrated before. Thanks to P2D model this coupling between electrochemical and thermal aspects may be easily done.
The total heat generated is the sum of all the reversible sources or sinks and the irreversible sources of heat into the cell.

$$Q_{tot} = Q_{irr} + Q_r \tag{3.42}$$

The irreversible contribution is given by ohmic losses in electrolyte and solid phase, activation over-potential and mass transport constraints.

$$Q_{irr} = i_l \cdot \nabla \cdot \Phi_l + i_s \cdot \nabla \cdot \Phi_s + (\nabla \cdot i_l) \cdot \eta \tag{3.43}$$

Instead, the reversible contribution is

$$Q_r = (\nabla \cdot i_l) \cdot T \cdot \frac{\partial E_{eq}}{\partial T} \tag{3.44}$$

Obviously, heat transfer occurs also with external environment, by conduction, convection and radiation. The general balance can be expressed as

$$\rho \cdot c_p \cdot \frac{\partial T}{\partial t} = Q_{tot} + \nabla \cdot (k_T \cdot \nabla \cdot T) - \nabla \cdot (h \cdot (T - T_a)) - \nabla \cdot (\sigma_T \cdot \epsilon_T \cdot (T^4 - T_a^4)) \tag{3.45}$$

where
ρ is the density (kg m^{-3})
c_p is the specific heat capacity at constant pressure (J kg^{-1} K^{-1})
k_T is the thermal conductivity (W m^{-1} K^{-1})
h is the heat transfer coefficient (W m^{-2} K^{-1})
σ_T is the Stefan Boltzmann constant $5.67 \cdot 10^{-8}$ W m^{-2} K^{-4}
ϵ_T is the emissivity
T_a is the ambient temperature (K)

3.4 Geometric parameters

For developing accurately the model, some parameters in equations described above have been acquired from experimental tests, other ones from literature or Comsol library.
In order to precisely model the geometry, all most relevant geometric parameters have been measured.

Material	Diameter [mm]	Thickness [mm]
Cu	18	0.0143
Graphite	18	0.0691
Celgard 2325	20	0.025
NMC	15	0.06
Al	15	0.018

Table 3.1: Graphite/NMC cell Geometric parameters

Material	Diameter [mm]	Thickness [mm]
Li	18	0.03
Celgard 2500	20	0.025
NMC	15	0.06
Al	15	0.018

Table 3.2: Lithium/NMC cell geometric parameters

3.5 Electrochemical parameters

3.5.1 Equilibrium electrode potential

The equilibrium potential, globally, may be seen as the skeleton on which other resistive contributions are added. Instead, locally, the equilibrium potential is seen depending on lithiation condition inside the cell [45].
For obtaining the real equilibrium potential curve, small charge and discharge pulses are applied to the cell and then, the battery rests for a period long enough to dissipate hysteresis effects. When polarization effects are totally disappeared the terminal voltage is close enough to open circuit voltage (OCV) [46]. Relaxation period in order to achieve a complete equilibrium takes a significant amount of time. So, for reducing time test, the OCV curve is obtained from slow galvanostatic cycling, C/25 in this case has been considered slow enough to simulate OCV behaviour [47]. Actually, the curve is defined correctly pseudo-OCV, because the system is never at open circuit.
First of all, graphite and NMC half cells are assembled; these kind of cells are composed by metallic lithium, the reference one, as negative electrode for both of them, commercial Celgard as separator, EC:DEC 1M 1:1 $LiPF_6$ as electrolyte and graphite gets the role of positive electrode for one cell and NMC622 is the cathode for the other. Considering that the equilibrium potential of the lithium is zero, being Li the reference electrode, the measurements achieved are referred to, respectively, graphite and NMC electrodes. Fig. 3.3 shows equilibrium potential trends.

The galvanostatic results are put in function of state of charge, because the equilibrium potential, as said before, depends on lithium concentration. For this reason the results are plotted against x, which is defined as the ratio between

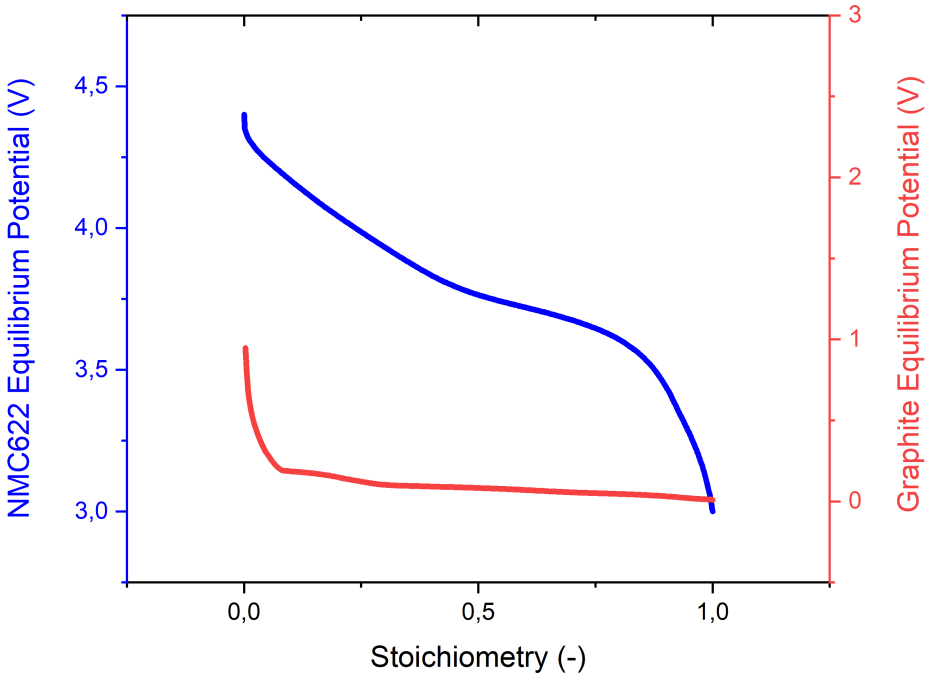

Figure 3.3: OCV curves of graphite and NMC622 half cell

lithium concentration in the active material at a certain instant and maximum lithium concentration. So, when the cell is fully charged the x assumes a value equal to 0, positive electrode is completely delithiated. During discharge the lithium concentration in the positive electrode increases up to its maximum value, at this point the ratio is equal to 1.

Ref. [48] reports graphite equilibrium potential curve whose value are very similar to that obtained in this work. Instead, any NMC622 equilibrium potential curve vs state of charge has not been found in literature, thus any comparison could not be conducted. In the library of *COMSOL Multiphysics* all data related to graphite as electrode material are included, therefore those data have been used to simulate electrochemical behaviour of the cell. The experimental tests for graphite have been anyway conducted to verify information reported in Comsol library.

3.5.2 Entropy coefficient

Electrode potentials depend on temperature, according to

$$E_{eq}^{T} = E_{eq} - (T - 298.15)\frac{\partial E_{eq}}{\partial T} \tag{3.46}$$

where
E_{eq}^{T} is the electrode potential at a certain temperature (V)
E_{eq} is the electrode potential at 298.15 K (V)
$\frac{\partial E_{eq}}{\partial T}$ is the entropy coefficient
Entropy coefficient is related to entropy variation by the equation

$$\frac{\partial E_{eq}}{\partial T} = \frac{\Delta S}{F} \tag{3.47}$$

ΔS values of NMC622, changing with SOC, have been extracted from literature [49]. By Eq. 3.47 entropy coefficient is derived

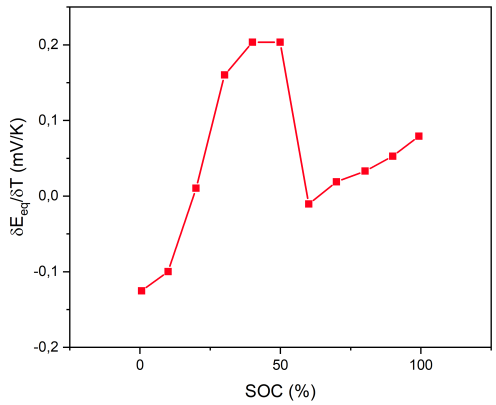

Figure 3.4: NMC622 entropy coefficient

3.5.3 Volume fraction of the active material in the electrode

An important parameter to estimate is surely volume fraction of active material inside electrodes which can take part in the reaction. For both electrode the value

is appraised by

$$c_{s,max} \cdot \epsilon_s \cdot d \cdot \Delta x \cdot F = i \cdot t \tag{3.48}$$

where
$c_{s,max}$ is the maximum concentration of lithium in the electrode (mol cm^{-3})
ϵ_s is the volume fraction of the solid phase
d is the thickness of the electrode (cm)
i is the current density (A cm^{-2})
F is the Faraday constant
t is the duration of discharge
The graphite and NMC622 half cells are charged and discharged at a current-rate of 0.1C. The duration of a discharge is evaluated accurately from experimental test; regarding the lithium concentration variation Δx during a completely discharge, x goes from 0 to 1, hence, $\Delta x = 1$.
Volume fraction for the NMC and graphite electrode are found to be respectively 0.3278 and 0.3335. The metallic lithium volume fraction is supposed to be 1.

3.5.4 Diffusion coefficient

The solid phase diffusion coefficient gets a key role in fast Li-ion transport, it determines the charge and discharge rate capability directly [50].
A GITT procedure is carried out on NMC half cells, composed as previously reported, in order to evaluate diffusion coefficient only for NMC electrode. In *Comsol* library the graphite diffusion coefficient is already available.
Previously, the cell is fully charged and discharged 3 times for activating it and then is charged again up to 4.4 V. After these preliminary procedures, GITT technique is performed, it consists of application of a current transient to change the SOC, followed by a relaxation period [48]. In this work, the discharge pulse is applied at 0.05C for 15 min and the rest period lasts 45 min, until the voltage reached its minimum value.

Fig. 3.5 shows an enlargement of what occurs between discharge pulse and rest period. At discharge pulse beginning the voltage drop follows a IR evolution, in this window the voltage rapidly decreases. After that, the decline is less steep. During the relaxation step the voltage raises again at first proportionally to IR and

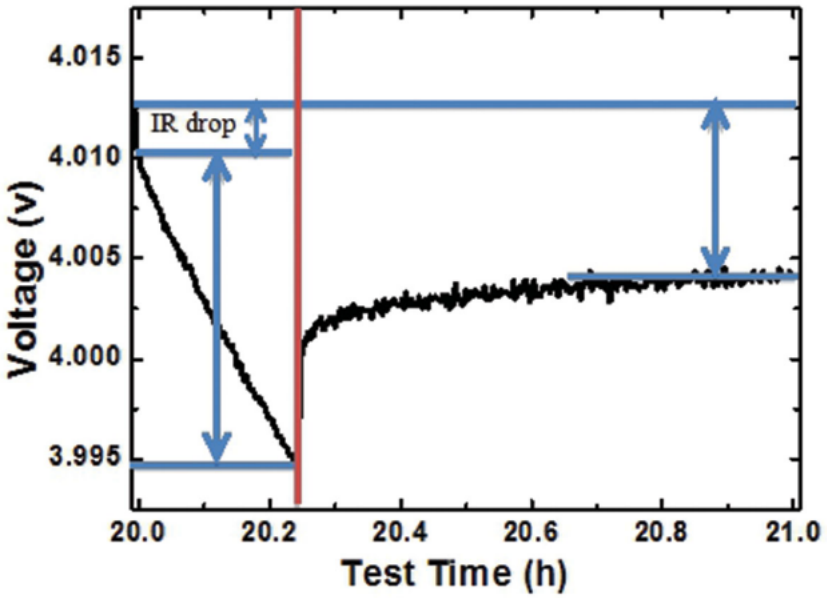

Figure 3.5: Voltage response of a GITT experiment. Red line divides the graph into two parts. The first one refers to discharge pulse and the second one to relaxation period

then slower.

As the cell is discharged at constant current, the voltage is function of time. Since double-layer charging and charge-transfer processes and any phase transformation are neglected, D_s can be evaluated by Fick's law [51].

$$D_s = \frac{4}{\pi} \cdot \left(\frac{IV_m}{z_A \cdot F \cdot S} \right)^2 \cdot \left[\frac{\partial E / \partial \delta}{\partial E / \partial \sqrt{t}} \right]^2 \tag{3.49}$$

where

F is the Faraday constant

S is the interfacial area between the electrode and the electrolyte (cm^2)

I is the current applied (A)

z_A is the charge number ($z_A = 1$ for Li-ions)

V_m is molar volume of the materials ($cm^3\ mol^{-1}$)

$\partial E/\partial \delta$ is the slope of the coulometric titration curve

$\partial E/\partial \sqrt{t}$ is the potential variation over the square root of time

This equation may be simplified considering the use of a low current rate for GITT,

hence the change of the steady-state voltage over a single galvanostatic titration is small. Moreover, if $\partial E/\partial\sqrt{t}$ shows a straight line behaviour over the entire time period of the current flux, Eq. 3.49 may be re-written as

$$D_s = \frac{4}{\pi \cdot \tau} \cdot \left(\frac{n \cdot V_m}{S}\right)^2 \cdot \left[\frac{\Delta E_s}{\Delta E_t}\right]^2 \tag{3.50}$$

where τ is the duration of each discharge step and n is the number of moles. Furthermore, considering all particles as spherically shaped with an equivalent radius R_p, the 3.51 gets

$$D_s = \frac{4}{\pi} \cdot \left(\frac{R_p}{3}\right)^2 \cdot \left[\frac{\Delta E_s}{\Delta E_t}\right]^2 \tag{3.51}$$

using the relationship

$$R_p = \frac{3\overline{V}}{\overline{S}} = \frac{\overline{R}^3}{\overline{R}^2} \tag{3.52}$$

where $\overline{S}$ and $\overline{V}$ are the average area and average volume of the particles and $\overline{R}$ is the radius of each particles.
The GITT is more accurate if the diffusion coefficient is evaluated at $0.2 \leq \delta \leq 0.5$, where δ is the ratio between the lithium concentration in the porous electrodes and maximum lithium concentration, out of which the discharge pulse can no longer be treated as a delta function [52]. By Eq. 3.52 a reference diffusion coefficient related to a reference temperature, T_{ref}=288.15 K, is obtained. The diffusion coefficient depends on temperature, since model takes into account the properties dependence on temperature, its variation is considered. Arrhenius's equation comes in handy

$$D_s = D_{s,ref} \exp\left[-\frac{E_a}{R}\left(\frac{1}{T} - \frac{1}{T_{ref}}\right)\right] \tag{3.53}$$

where E_a is the NMC energy activation whose value is related to a δ=0.5 and equals to 0.457 eV. The Fig. 3.6 displays diffusion coefficient at different temperatures.

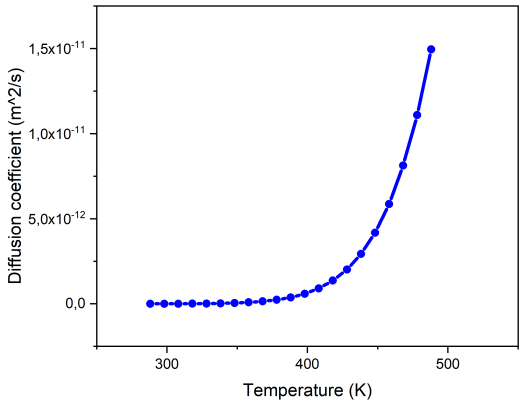

Figure 3.6: Diffusion coefficient dependence on temperature

3.5.5 Exchange current density

Another important parameter in the P2D model is the exchange current density. This parameter gives information about rates of electron transfer as the ions migrate between electrolyte and electrode and is the current measured at zero over potential as well. The value is obtained from charge transfer resistance whose value is measured by EIS. Butler-Volmer relationship

$$j = j_0 \cdot \left(\exp\left[\frac{(1-\alpha) \cdot F \cdot \eta}{R \cdot T} \right] - \exp\left[\frac{-\alpha \cdot F \cdot \eta}{R \cdot T} \right] \right) \tag{3.54}$$

can be linearized if the over potential is small. Hence,

$$j = j_0 \cdot \frac{F \cdot \eta}{R \cdot T} \tag{3.55}$$

Charge transfer resistance is defined as

$$R_{ct} = \frac{\eta}{j \cdot S} \tag{3.56}$$

where S is the electrode-electrolyte interface surface area. Combining 3.55 and 3.56 is found

$$j_0 = \frac{R \cdot T}{R_{ch} \cdot S \cdot F} \tag{3.57}$$

EIS test is performed in potentiostatic mode with a voltage amplitude of 10 mV, in the frequency range of 10 mHz to 500 kHz. The measurements are carried out for both electrodes, thus two half cells are assembled. EIS results are recorded at 50% SOC and at different temperatures, 25°C, 30°C, 40°C, 50°C and 60°C. The curves are fitted using equivalent circuit displayed in Fig. 3.7 where R1 is the electrolyte resistance that ions bump into, R2 and CPE1 describe charge transfer through SEI layer, instead R3 and CPE2 fit data related to charge transfer at active material/electrolyte interface. CPE3 models behaviour at low frequency, referred to diffusion processes.

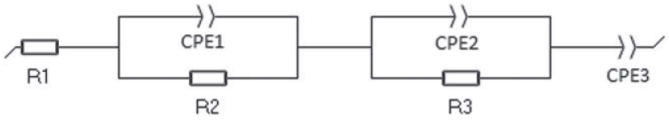

Figure 3.7: Equivalent circuit used to fit reaction rate data

EIS measurements are shown in Tab. 3.3. For NMC half cell the first small semi-circle located at high frequencies does not change a lot with temperature. On the other hand, the radius of the second one at middle frequencies decreases with increasing temperature, this is caused by a R3 reduction.

Electrode		25 °C	30 °C	40 °C	50 °C	60 °C
NMC	R_3 (Ω)	7.358	3.985	1.021	0.6308	0.578
	j_0 (A/m^2)	4.94	9.27	37.39	62.52	70.23
Graphite	R_3 (Ω)	124.9	71.88	31.97	16.47	10.11
	j_0 (A/m^2)	0.202	0.357	0.829	1.661	2.789

Table 3.3: Fitting results

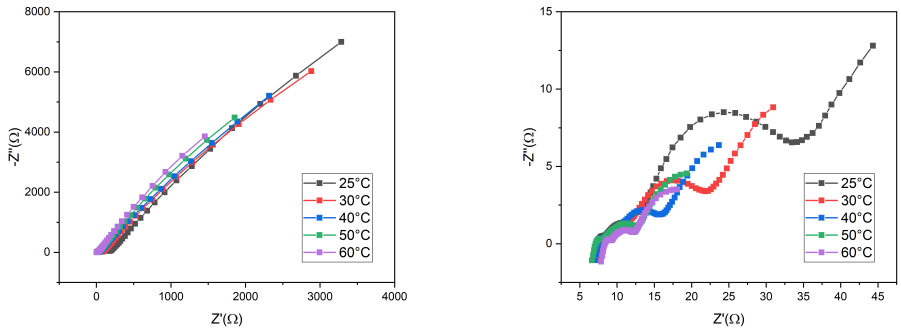

(a) Lithium/NMC622 (b) Lithium/NMC622

Figure 3.8: Impedance variation with temperature

3.5.6 Particle radius

Field emission scanning electron microscopy (FESEM) has been employed to evaluate particle radius of NMC material. An average value has been deduced from FESEM picture, considering the heterogeneous pattern material. The particle radius of the NMC obtained is 6.9 μm.

3.5.7 Parameters from literature

Maximum li-ion concentration in the NMC material and its electrical conductivity are the ones in [53]. The electrolyte parameters, as transport number, diffusion coefficient and electrical conductivity are suggested by software Comsol. Moreover, diffusion coefficient, entropy coefficient and electrical conductivity of graphite material such as aluminum and copper electrical conductivity proposed by Comsol are taken in account. The tables shown below summarize some of these parameters

3.6 Thermal parameters

Thermal conductivity (K) is an anisotropic parameter caused by stacking of cell layers. Eq. 3.58 gives thermal conductivity contribution along surfaces, instead Eq.

	Graphite	NMC622	$LiPF_6$	Li
Maximum concentration [mol m^3]	31370	59493		77078
Electrical conductivity [S m^{-1}]	100	0.17	0.771	$10.8 \cdot 10^6$
Initial electrolyte [mol m^3]			1000	
Transport number			0.363	

Table 3.4: Parameters from literature and Comsol library

	Aluminum	Copper
Electrical conductivity [S m^{-1}]	$3.77 \cdot 10^7$	$5.99 \cdot 10^7$

Table 3.5: Parameters from literature and Comsol library

3.59 gives thermal conductivity value along battery thickness.

$$K_{\parallel} = \frac{L_{NC} \cdot K_{NC} + L_{NE} \cdot K_{NE} + L_S \cdot K_S + L_{PE} \cdot K_{PE} + L_{PC} \cdot K_{PC}}{L_{tot}} \tag{3.58}$$

$$\frac{L_{tot}}{K_{\perp}} = \frac{L_{NC}}{K_{NC}} + \frac{L_{NE}}{K_{NE}} + \frac{L_S}{K_S} + \frac{L_{PE}}{K_{PE}} + \frac{L_{PC}}{K_{PC}} \tag{3.59}$$

Eqs. 3.58 and 3.59 are a little bit modified for evaluating, respectively, parallel and perpendicular contribution of lithium/NMC cells. The term related to negative current collector disappears since copper collector is missing in this type of cell. Thermal conductivity of components are taken from Comsol library and due to lack of data in literature about NMC622 as positive electrode in lithium-ion batteries, NMC811 thermal conductivity is used as it is in software library. The same is done for Celgard 2325, whose parameters have been supposed equal to Celgard 2500 ones. Thermal conductivity values are shown below (Tab. 3.6 and 3.7).
The density (ρ) and the specific heat capacity (C_p) are measured as a volume average of the different cell layers.

$$\rho = \frac{\sum_i \rho_i \cdot V_i}{V_{tot}} \tag{3.60}$$

$$C_p = \frac{\sum_i c_{p,i} \cdot V_i}{V_{tot}} \tag{3.61}$$

	Aluminum	NMC622	Celgard2325	Graphite	Copper	$K_{\parallel}$	$K_{\perp}$
Thermal conductivity [W m^{-1} K^{-1}]	238	1.58	1.21	4.21	400	54.71	1.46

Table 3.6: Thermal conductivity of graphite/NMC622 components

	Aluminum	NMC622	Celgard2500	Lithium	$K_{\parallel}$	$K_{\perp}$
Thermal conductivity [W m^{-1} K^{-1}]	238	1.58	1.21	84.8	52.27	2.25

Table 3.7: Thermal conductivity of lithium/NMC622 components

Tab. 3.8 summarizes density and heat capacity of all components.

	Aluminum	NMC622	Celgard2325	Celgard2500	Lithium	Graphite	Copper
Density [kg m^{-3}]	2700	4.87	1043	1043	535	2270	8960
Heat capacity [J kg^{-1} K^{-1}]	900	840.1	1688	1688	3582	881	385

Table 3.8: Density and heat capacity of both lithium/NMC622 and graphite/NMC622 components

3.7 Model results and validation

All the electrochemical and thermal parameters evaluated above are inserted in the Comsol code as input. For comparing model polarization curves and experimental ones, coin cells have been assembled and cycled at different current rate, specifically at C/10, C/5 and C/2. The Comsol codes have been runned at the same conditions in order to compare the results.

3.7.1 Electrochemical validation

Figures below display charge and discharge polarization curve at C/10, C/5 and C/2. The trend of both curves, experimental and model, is similar enough, especially

at lower current rate. On the other hand, lithium/NMC622 coin cells cycled at C/2, Fig. 3.11(b), shows a faster capacity fade and degradation, and in fact the charge and discharge time is shorter than that of the model, even if the model initial capacity is the same of experimental one.

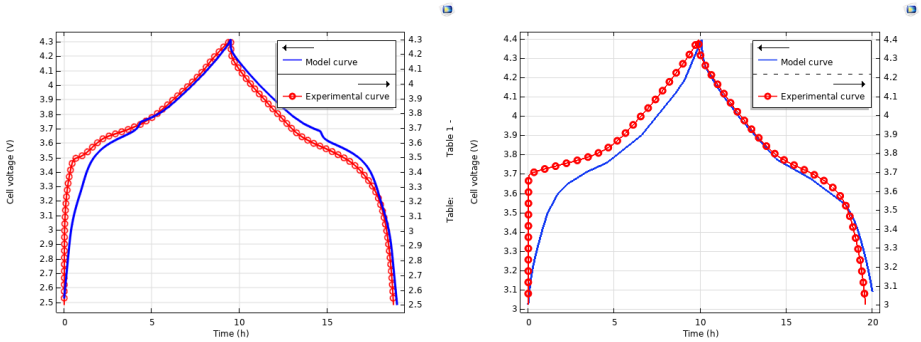

(a) Graphite/NMC622 (b) Lithium/NMC622

Figure 3.9: Model and experimental voltage profiles at C/10

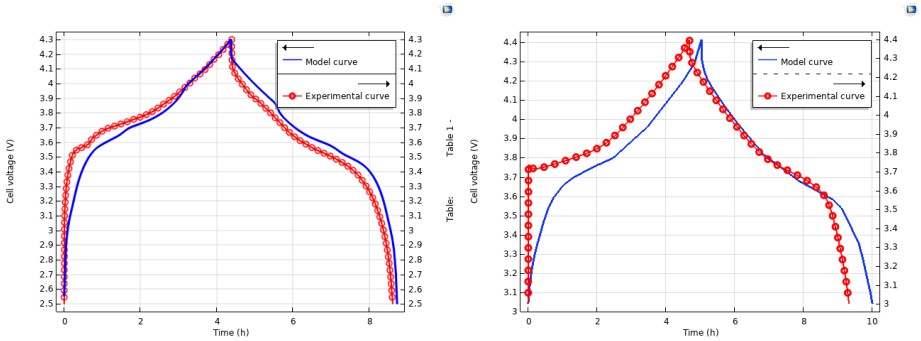

(a) Graphite/NMC622 (b) Lithium/NMC622

Figure 3.10: Model and experimental voltage profiles at C/5

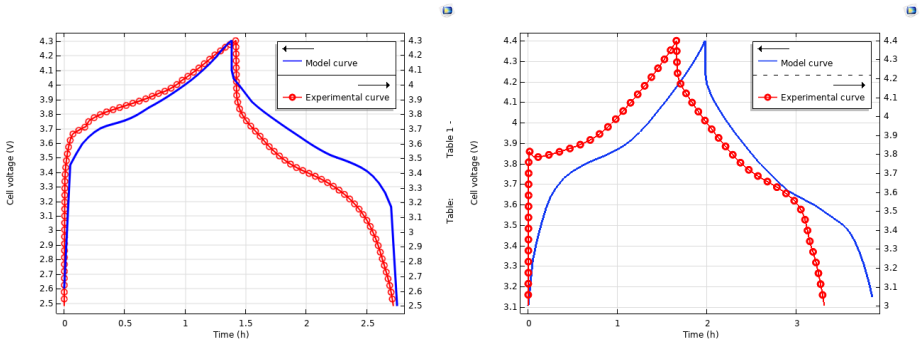

(a) Graphite/NMC622 (b) Lithium/NMC622

Figure 3.11: Model and experimental voltage profiles at C/2

3.7.2 Thermal validation

In this section the thermal results are analyzed. But first of all, a summary of main sources of heat inside cells is appropriate. The transport of ions from one porous electrode to another is the source of irreversible heat. It is interesting to notice that the heat contribution is different between charge and discharge due to electrolyte properties dependence on concentration and temperature such as diffusivity and conductivity. In current collectors region the only source of heat has an ohmic nature by electrons conduction from tabs to electrodes. In the electrodes region the heat generation has both reversible and irreversible contribution. The lithium intercalation and deintercalation bring changes in the electrodes crystalline structure, but it can be both endothermic and exothermic. The entropy factor takes into account this phenomenon. The irreversible heat contribution is ascribed to solid phase diffusion and kinetics of reaction, which are exothermic processes.
In contrast to electrochemical part, it has not been possible to validate the thermal behaviour. Despite that, it is interesting to analyze thermal results. The cells are charged and discharged at different current rate, as done in the electrochemical part. At the beginning the cells are at room temperature, 298.15 K. As boundary condition a natural air convection cooling (heat transfer coefficient h=3.5 W m^{-1} K^{-1} and air temperature 298.15 K) is simulated.
Looking at Figs. 3.12, 3.13, 3.14, it is clear that the generated heat is less at lower current rate, leading to a little temperature growth compared to ambient temperature. At the beginning of graphite/NMC charging a small cooling effect is

visible, Fig. 3.15. This phenomenon is also reported in other studies [[54], [49]] and can be explained by entropy change at low SOC during Li^+ deintercalation of the NMC and the following intercalation of the graphite, processes more energy demanding. Exothermic and endothermic processes do not balance each other out, but heat sinks seem to prevail for a short period. Irreversible sources due to diffusion and conduction resistance generate peaks in the heat flow rate at the end of discharge and in fact a re-increase in temperature can be seen for SOC lower than 5-10 %.
Reversible heat generated into lithium anode is not an important source of heat, for this the entropy coefficient has been neglected. Probably due to nature of the lithium arrangement in NMC622 electrode, the total reversible heat during charging is more endothermic than discharging, which is more exothermic. So, for this reason at C/10 and C/5 the temperature decreases for a while, as could be seen in Fig. 3.16. Since reversible heat does not depend on C-rate, while irreversible heat increases to C-rate growth, the endothermic effects totally disappear at C/2 and 1C.

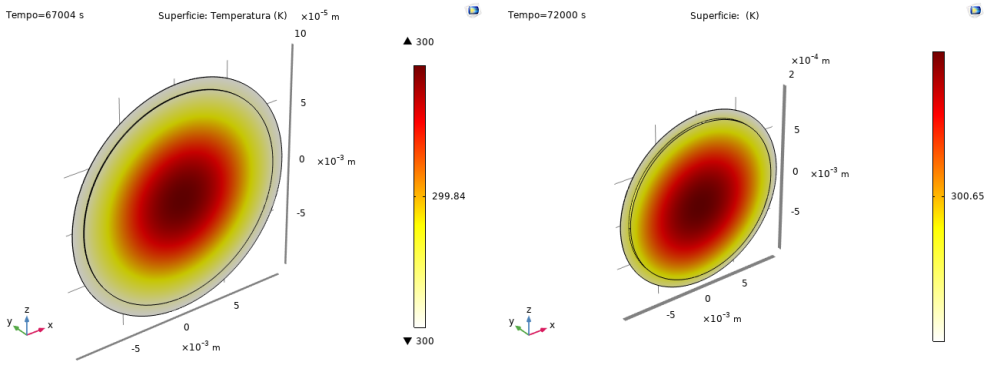

(a) Graphite/NMC622 (b) Lithium/NMC622

Figure 3.12: Temperature distribution after a cycle at C/10

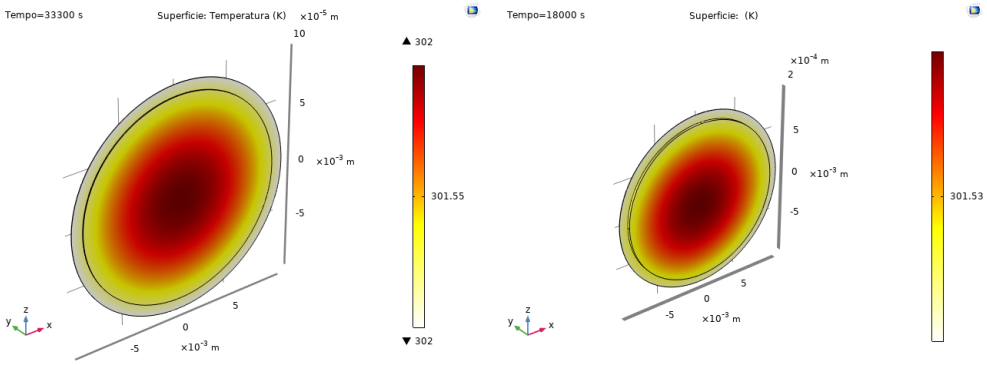

(a) Graphite/NMC622 (b) Lithium/NMC622

Figure 3.13: Temperature distribution after a cycle at C/5

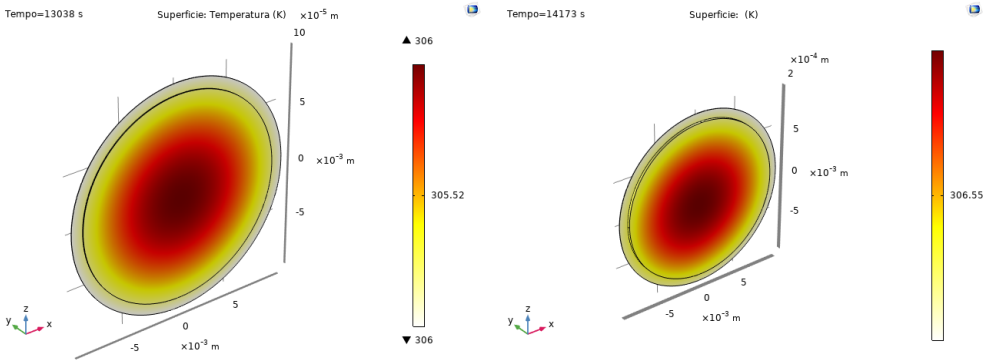

(a) Graphite/NMC622 (b) Lithium/NMC622

Figure 3.14: Temperature distribution after a cycle at C/2

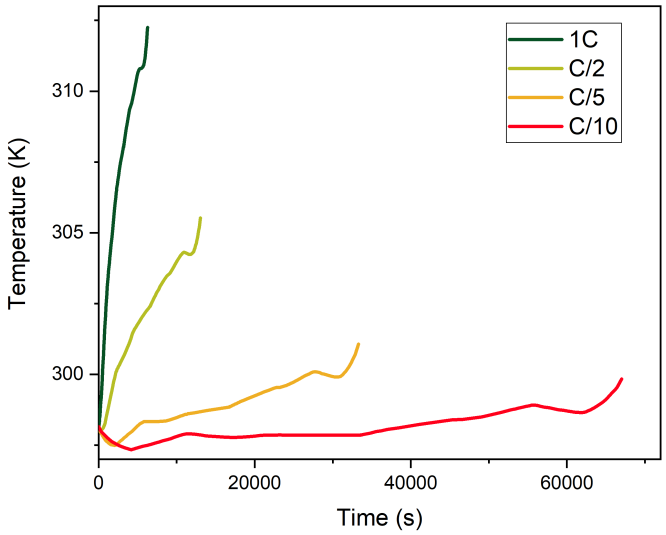

Figure 3.15: Graphite/NMC-Temperature trend over time

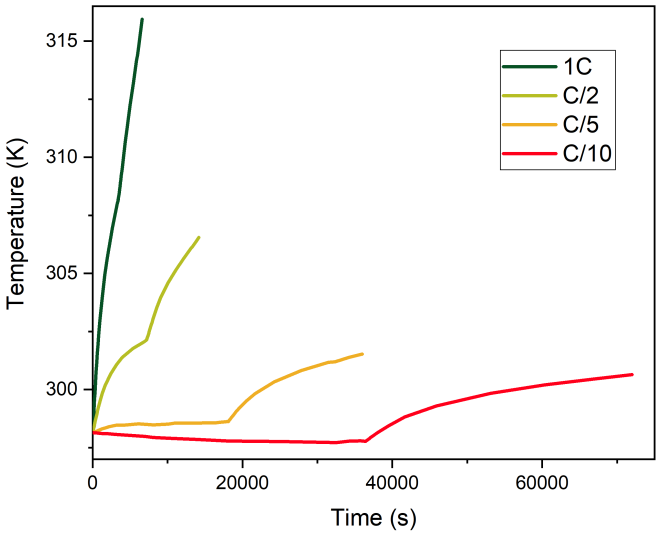

Figure 3.16: Lithium/NMC-Temperature trend over time

Chapter 4

Other tests

4.1 T-cell results

EIS technique is a powerful tool to investigate the relationship between crystal lattice and electrochemical properties of the cell. A T-cell has been assembled as explained in subsection 1.4.2, where the lithium foil acts as reference electrode in impedance measurements. EIS measurements have been carried out after each full cycle at C/10, in order to evaluate internal changing over operations. The impedance measurements are performed between 100 kHz and 10 mHz, in whom main electrochemical processes are visible.

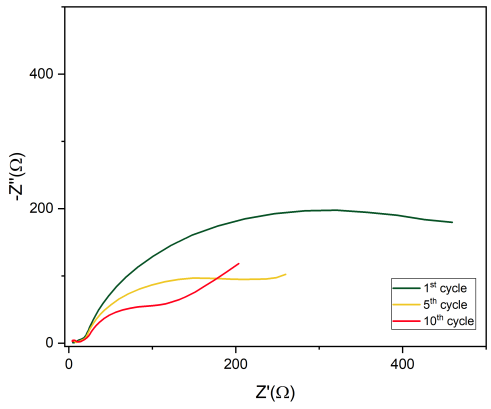

Figure 4.1: Impedance measurements after 1^{st}, 5^{th} and 10^{th} cycle

The radius of semicircle appeared in the middle-low frequency range, Fig. 4.1, decreases with the number of cycle, revealing a decrease of the charge-transfer resistance across electrode materials. One reason applied to explain the phenomena is that ionic conductivity of the materials increases, probably due to a more stable SEI. In fact, the difference in radius between the first cycle and the fifth one is larger than that between the fifth cycle and the tenth, a sign that the passivating film forms mostly during the first charge/discharge process and is stable during the latter charge/discharge cycles. Fifth and tenth cycle show at lower frequencies the beginning of a diffusive tail, related to lithium ion diffusion across cathode material. Surly, increasing frequency range, all these processes would be better seen. Moreover, the frequency domain of impedance response of SEI is usually found to overlap with that of the inductive component, which can not be seen, as well as the electrolyte resistance. Fig. 4.2 and Fig. 4.3 show, respectively, EEC used to fitting impedance data and fitting results.

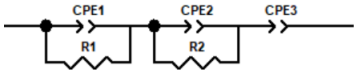

Figure 4.2: EEC used to fit T-cell impedance data

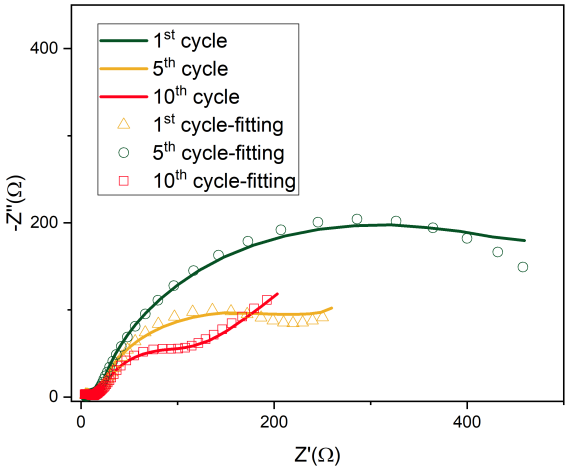

Figure 4.3: Fitting results

Chapter 5

Conclusions

The goal of this work is that of knowing better and optimizing lithium-ions batteries technology, in order to boost the deployment of this kind of batteries in the electric vehicles market.
The capacity fade of commercial NMC coin cells is studied as a function of time and storage state of charge. In general, a faster degradation and increase in impedance with time is evident at high SOC. Unfortunately, the temperature effects are not taken into account due to lack of equipment. Impedance curve is fitted by an equivalent circuit model whose components represent series and polarization resistance, capacitive phenomena and diffusion processes. By fitting, the changes of these parameters with time are evaluated. An increase in ohmic resistance such as in parallel resistance is seen with storage time. On the contrary the depression factor decreases because of a growth of the polarization semi-circle as well as an increase in time constant of polarization. The trend of some of these parameters is not so clear due to the short analysis time, only 30 days; in literature calendar aging is studied for certainly longer period. The results of calendar aging have shown a strong influence by characterization procedure and SOC resetting. In fact, a faster capacity fade is noticed in coin cells characterized every 6 days and/or re-charged up to SOC 100 %. Obviously, the real battery lifetime without any electrochemical characterization is longer than that estimated in this study.
The Comsol model foretells the thermal and electrochemical behaviour of the lithium-ions battery over a wide range of C-rates and number of cycles. It is considered a powerful tool for optimizing NMC cells, evaluating cell performances

and forecasting design or thermal issues before actual creation of coin cells in laboratory. Moreover, this model could be easily conformed to other lithium-ion types, changing electrode and electrolyte materials. Due to lack of information in literature about both NMC622 as cathode and metallic lithium as anode some approximations have been done for developing this model. Some parameters referring to NMC662 have been assumed equals to NMC811 ones, material more employed in lithium batteries market. Regarding metallic lithium, lithium insertion equations, in place of Butler-Volmer equations, govern particles intercalation at anodic side. Anyway Li anode is considered as a porous electrode, neglecting entropy factor changes, but these assumptions have not been possible to compare with other studies. Two important achievements in this thesis are the integration of SEI formation and 3D thermal analysis, thanks to them the model gives more truthful information about actual cell behaviour and takes in consideration the effects of temperature on cell parameters as well. Finally, future works could validate thermal analysis and try to include SEI layer growth on metallic lithium surface.

Bibliography

[1] Xing Luo, Jihong Wang, Mark Dooner, and Jonathan Clarke. «Overview of current development in electrical energy storagetechnologies and the application potential in power system operation». In: *Applied Energy* 137 (2014), pp. 511–536 (cit. on p. 1).

[2] Helder Lopes Ferreira, Raquel Garde, Gianluca Fulli, Wil Kling, and Joao Pecas Lopes. «Characterisation of electrical energy storage technologies». In: *Energy* 53 (2013), pp. 288–298 (cit. on p. 1).

[3] Boucar Diouf and Ramchandra Pode. «Potential of lithium-ion batteries in renewable energy». In: *Renewable Energy* 76 (2015), pp. 375–380. URL: `https://doi.org/10.1016/j.renene.2014.11.058` (cit. on p. 1).

[4] X. Yuan, H. Liu, and J. Zhang. *Lithium-Ion Batteries - Advanced Materials and Technologies*. Taylor Francis Group, 2011 (cit. on pp. 3, 4).

[5] J.M. Tarascon and M. Armand. «Issues and challenges facing rechargeable lithium batteries». In: *Nature* 414 (2001), pp. 359–367 (cit. on p. 4).

[6] Lei Wang, Ziyue Zhou, Xiao Yan, Feng Hou, Lei Wen, Wenbin Luo, Ji Liang, and Shi Xue Dou. «Engineering of lithium-metal anodes towards a safe and stable battery». In: *Energy Storage Materials* 14 (2018), pp. 22–48 (cit. on p. 5).

[7] Lin D., Liu Y., and Cui Y. «Reviving the lithium metal anode for high-energy batteries». In: *Nature Nanotech* 12 (2017), pp. 194–206 (cit. on p. 5).

[8] E. Antolini. «$LiCoO_2$: formation, structure, lithium and oxygen nonstoichiometry, electrochemical behaviour and transport properties». In: *Solid State Ionics* 170 (2004), pp. 159–171 (cit. on p. 5).

[9] G.G. Amatucci, J.M. Tarascon, and L.C. Klein. «Cobalt dissolution in $LiCoO_2$-based non-aqueous rechargeable batteries». In: *Solid State Ionics* 83 (1996), pp. 167–173 (cit. on p. 6).

[10] M. Stanley Whittingham. «Lithium Batteries and Cathode Materials». In: *Chemical Reviews* 104 (2004), pp. 4271–4302. DOI: https://doi.org/10.1021/cr020731c (cit. on p. 6).

[11] Li Wang, Jiangang Li, Xiangming He, Weihua Pu, Chunrong Wan, and Changyin Jiang. «Recent advances in layered $LiNi_xCo_yMn_{1xy}O2$ cathode materials for lithium ion batteries». In: *Journal of Solid State Electrochemistry* 13 (2008), pp. 1157–1164. DOI: https://doi.org/10.1007/s10008-008-0671-7 (cit. on p. 6).

[12] Sébastien Patoux, Lise Daniel, Carole Bourbon, Hélène Lignier, Carole Pagano, Frédéric Le Cras, Séverine Jouanneau, and Sébastien Martinet. «High voltage spinel oxides for Li-ion batteries: From the material research to the application». In: *Journal of Power Sources* 189 (2009), pp. 344–352. DOI: https://doi.org/10.1016/j.jpowsour.2008.08.043 (cit. on p. 7).

[13] Jeffrey W. Fergus. «Recent developments in cathode materials for lithium ion batteries». In: *Journal of Power Sources* 195 (2010), pp. 939–954 (cit. on p. 7).

[14] Z. Tian, H. Yu, Z. Zhang, and X. Xu. «Performance improvements of cobalt oxide cathodes for rechargeable lithium batteries». In: *ChemBioEng Rev* 5 (2018), pp. 111–118. URL: https://doi.org/10.1002/cben.201700008 (cit. on p. 7).

[15] J. Vetter et al. «Ageing mechanisms in lithium-ion batteries». In: *Journal of Power Sources* 147 (2005), pp. 269–281. URL: https://doi.org/10.1016/j.jpowsour.2005.01.006 (cit. on pp. 15–17, 40).

[16] Doron Aurbach, Ella Zinigrad, Yaron Cohen, and Hanan Teller. «A short review of failure mechanisms of lithium metal and lithiated graphite anodes in liquid electrolyte solutions». In: *Solid State Ionics* 148 (2002), pp. 405–416. DOI: https://doi.org/10.1016/S0167-2738(02)00080-2 (cit. on p. 15).

[17] Jun Li, Edward Murphy, Jack Winnick, and Paul A Kohl. «The effects of pulse charging on cycling characteristics of commercial lithium-ion batteries». In: *Journal of Power Sources* 102 (2001), pp. 302–309. DOI: https://doi.org/10.1016/S0378-7753(01)00820-5 (cit. on p. 15).

[18] A.M Andersson, Kristina Edström, and John Oswald Thomas. «Characterisation of the ambient and elevated temperature performance of a graphite electrode». In: *Journal of Power Sources* 82 (1999), pp. 8–12 (cit. on p. 15).

[19] M. N. Richard and J. R. Dahn. «Accelerating Rate Calorimetry Study on the Thermal Stability of Lithium Intercalated Graphite in Electrolyte. I. Experimental». In: *Journal of The Electrochemical Society* 146 (1999), p. 2068 (cit. on p. 16).

[20] Julius Schmitt, Arpit Maheshwari, Michael Heck, Stephan Lux, and Matthias Vetter. «Impedance change and capacity fade of lithium nickel manganese cobalt oxide-based batteries during calendar aging». In: *Journal of Power Sources* 353 (2017), pp. 183–194. URL: https://doi.org/10.1016/j.jpowsour.2017.03.090 (cit. on pp. 18, 24, 26).

[21] Madeleine Ecker, Jochen B. Gerschler, Jan Vogel, Stefan Käbitz, Friedrich Hust, Philipp Dechent, and Dirk Uwe Sauer. «Development of a lifetime prediction model for lithium-ion batteries based on extended accelerated aging test data». In: *Journal of Power Sources* 215 (2012), pp. 248–257. URL: https://doi.org/10.1016/j.jpowsour.2012.05.012 (cit. on pp. 18, 24).

[22] Minggao Ouyang, Zhengyu Chu, Languang Lu, Jianqiu Li, Xuebing Han, Xuning Feng, and Guangming Liu. «Low temperature aging mechanism identification and lithium deposition in a large format lithium iron phosphate battery for different charge profiles». In: *Journal of Power Sources* 286 (2015), pp. 309–320. URL: https://doi.org/10.1016/j.jpowsour.2015.03.178 (cit. on p. 18).

[23] Quan-Chao Zhuang, Xiang-Yun Qiu, Shou-dong Xu, Ying-Huai Qiang, and Shi-Gang Sun. *Lithium-Ion Batteries - New Developments*. InTech, 2012 (cit. on p. 23).

[24] B. Stiaszny, J. C. Ziegler, E. E. Krau, M. Zhang, J. P. Schmidt, and E. Ivers-Tiffée. «Electrochemical characterization and post-mortem analysis of aged LiMn 2O4-NMC/graphite lithium ion batteries part II: Calendar aging». In: *Journal of Power Sources* 258 (2014), pp. 61–75 (cit. on p. 24).

[25] M. Broussely, P. Biensan, F. Bonhomme, P. Blanchard, S. Herreyre, K. Nechev, and R. J. Staniewicz. «Main aging mechanisms in Li ion batteries». In: *Journal of Power Sources* 146 (2005), pp. 90–96 (cit. on p. 24).

[26] Sean M. Wood, Chengcheng Fang, Eric J. Dufek, Shrikant C. Nagpure, Sergiy V. Sazhin, Boryann Liaw, and Y. Shirley Meng. «Predicting Calendar Aging in Lithium Metal Secondary Batteries: The Impacts of Solid Electrolyte Interphase Composition and Stability». In: *Advanced Energy Materials* 8 (2018). DOI: https://doi.org/10.1002/aenm.201801427 (cit. on p. 25).

[27] Peter Keil, Simon F. Schuster, Jorn Wilhelm, Julian Travi, Andreas Hauser, Ralph C. Karl, and Andreas Jossen. «Calendar Aging of Lithium-Ion Batteries». In: *Journal of Electrochemical Society* 163 (2016), A1872–A1880 (cit. on p. 25).

[28] Jean-Baptiste Jorcin, Mark E. Orazem, Nadine Pébère, and Bernard Tribollet. «CPE analysis by local electrochemical impedance spectroscopy». In: *Electrochimica Acta* 51 (2006), pp. 1473–1479 (cit. on p. 29).

[29] Barbara Stiaszny, Jörg C. Ziegler, Elke E. Krauß, Mengjia Zhang, Jan P. Schmidt, and Ellen Ivers-Tiffée. «Electrochemical characterization and post-mortem analysis of aged LiMn2O4–NMC/graphite lithium ion batteries part II: Calendar aging». In: *Journal of Power Sources* 258 (2014), pp. 61–75 (cit. on p. 29).

[30] Wladislaw Waag, Stefan Käbitz, and Dirk Uwe Sauer. «Experimental investigation of the lithium-ion battery impedance characteristic at various conditions and aging states and its influence on the application». In: *Applied Energy* 102 (2013), pp. 885–897 (cit. on p. 29).

[31] Arpit Maheshwari, Michael Heck, and Massimo Santarelli. «Cycle aging studies of lithium nickel manganese cobalt oxide-based batteries using electrochemical impedance spectroscopy». In: *Electrochimica Acta* 273 (2018), pp. 335–348 (cit. on p. 31).

[32] Matthew T. Lawder, Bharatkumar Suthar, Paul W. C. Northrop, Sumitava De, C. Michael Hoff, Olivia Leitermann, Mariesa L. Crow, Shriram Santhanagopalan, and Venkat R. Subramanian. «Battery Energy Storage System (BESS) and Battery Management System (BMS) for Grid-Scale Applications». In: *Proceedings of the IEEE* 102.6 (2014), pp. 1014–1030. DOI: 10.1109/JPROC.2014.2317451 (cit. on p. 34).

[33] P. W. C. Northrop, B. Suthar, V. Ramadesigan, S. Santhanagopalan, R. D. Braatz, and V. R. Su. «Efficient simulation and reformulation of lithium-ion battery models for enabling electric transport». In: *Journal of the Electrochemical Society* 161 (2014). DOI: 10.1149/2.018408jes (cit. on p. 34).

[34] Ali Jokar, Barzin Rajabloo, Martin Désilets, and Marcel Lacroix. «Review of simplified Pseudo-two-Dimensional models of lithium-ion batteries». In: *Journal of Power Sources* 327 (2016), pp. 44–55. DOI: https://doi.org/10.1016/j.jpowsour.2016.07.036 (cit. on p. 35).

[35] Thomas K.E., Newman J., and Darling R.M. *Advances in Lithium-Ion Batteries*. Springer, Boston, MA, 2002, pp. 345–392 (cit. on p. 36).

[36] Marc Doyle, Thomas F. Fuller, and John Newman. «The importance of the lithium ion transference number in lithium/polymer cells». In: *Electrochimica Acta* 39 (1994), pp. 2073–2081. DOI: https://doi.org/10.1016/0013-4686(94)85091-7 (cit. on p. 37).

[37] Meng Xu, Benjamin Reichman, and Xia Wang. «Modeling the effect of electrode thickness on the performance of lithium-ion batteries with experimental validation». In: *Energy* 186 (2019). DOI: https://doi.org/10.1016/j.energy.2019.115864 (cit. on p. 37).

[38] Gang Ning, Ralph E. White, and Branko N. Popov. «A generalized cycle life model of rechargeable Li-ion batteries». In: *Electrochimica Acta* 51 (2006), pp. 2012–2022 (cit. on p. 40).

[39] Hong-Li Zhang, Feng Li, Chang Liu, Jun Tan, and Hui-Ming Cheng. «New insight into the solid electrolyte interphase with use of a focused ion beam». In: *The journal of physical chemistry* 109 (2005), pp. 22205–22211. DOI: https://doi-org.ezproxy.biblio.polito.it/10.1021/jp053311a (cit. on p. 40).

[40] Ping Liu, John Wang, Jocelyn Hicks-Garner, Elena Sherman, Souren Soukiazian, Mark Verbrugge, Harshad Tataria, James Musser, and Peter Finamore. «New insight into the solid electrolyte interphase with use of a focused ion beam». In: *Journal of the electrochemical society* 157 (2010), A499–A507 (cit. on p. 40).

[41] Henrik Ekström and Göran Lindbergh. «A model for predicting capacity fade due to SEI formation in a commercial Graphite/$LiFePO_4$ cell». In: *Journal of the electrochemical society* 162 (2015), A1003–A1007 (cit. on p. 40).

[42] Jason B. Siegel, Anna G. Stefanopoulou, Patrick Hagans, Yi Ding, and David Gorsich3. «Expansion of lithium ion pouch cell batteries: observations from neutron imaging». In: *Journal of the electrochemical society* 160 (2013), A1031 (cit. on p. 42).

[43] Guifang Guo, Bo Long, Bo Cheng, Shiqiong Zhou, Peng Xu, and Binggang Cao. «Three-dimensional thermal finite element modeling of lithium-ion battery in thermal abuse application». In: *Journal of Power Sources* 195 (2010), pp. 2393–2398 (cit. on p. 44).

[44] Todd M. Bandhauer, Srinivas Garimella, and Thomas F. Fuller. «A Critical Review of Thermal Issues in Lithium-Ion Batteries». In: *Journal of The Electrochemical Society* 158 (2011), R1–R25 (cit. on p. 44).

[45] Nicolas Dufour, Marion Chandesris, Sylvie Genies, Mikael Cugnet, and Yann Bultel. «Lithiation heterogeneities of graphite according to C-rate and mass-loading: A model study». In: *Electrochimica Acta* 272 (2018), pp. 97–107 (cit. on p. 46).

[46] Dong Feng, Jun Huang, Peng Jin, Haitao Chen, Anyuan Wang, and Minxin Zheng. «Parameter Identification and Dynamic Simulation of Lithium-Ion Power Battery Based on DP Model». In: *2019 14th IEEE Conference on Industrial Electronics and Applications (ICIEA)* (2019), pp. 1285–1289. DOI: 10.1109/ICIEA.2019.8833993 (cit. on p. 46).

[47] G. B. Less et al. «Micro-Scale Modeling of Li-Ion Batteries: Parameterization and Validation». In: *Journal of The Electrochemical Society* 159.6 (2012), A697 (cit. on p. 46).

[48] Chang-Hui Chen, Ferran Brosa Planella, Kieran O'Regan, Dominika Gastol, W. Dhammika Widanage, and Emma Kendrick. «Development of Experimental Techniques for Parameterization of Multiscale Lithium-ion Battery Models». In: *Journal of The Electrochemical Society* 167 (2020). DOI: https://doi.org/10.1149/1945-7111/ab9050 (cit. on pp. 47, 49).

[49] Ralph E. Williford, Vilayanur V. Viswanathan, and Ji-Guang Zhang. «Effects of entropy changes in anodes and cathodes on the thermal behavior of lithium ion batteries». In: *Journal of Power Sources* 189 (2009), pp. 101–107 (cit. on pp. 48, 59).

[50] Suihan Cui et al. «Optimized Temperature Effect of Li-Ion Diffusion with Layer Distance in $Li(Ni_xMn_yCo_z)O_2$ Cathode Materials for High Performance Li-Ion Battery». In: *Advanced Energy Materials* 6 (2016). DOI: 10.1002/aenm.201501309 (cit. on p. 49).

[51] W. Weppner and R. A. Huggins. «Determination of the Kinetic Parameters of Mixed-Conducting Electrodes and Application to the System Li_3Sb». In: *Journal of The Electrochemical Society* 124 (1977) (cit. on p. 50).

[52] Zheng Shen1, Lei Cao, Christopher D. Rahn, and Chao-Yang Wang. «Least Squares Galvanostatic Intermittent Titration Technique (LS-GITT) for Accurate Solid Phase Diffusivity Measurement». In: *Journal of The Electrochemical Society* 160 (2013), A1842 (cit. on p. 51).

[53] Alexander W. Abboud, Eric J. Dufek, and Boryann Liaw. «Communication—Implications of Local Current Density Variations on Lithium Plating Affected by Cathode Particle Size». In: *Journal of The Electrochemical Society* 166 (2019), A667 (cit. on p. 54).

[54] Wenjiao Zhao, Magnus Rohde, Ijaz Ul Mohsin, Carlos Ziebert, and Hans J. Seifert. «Heat Generation in NMC622 Coin Cells during Electrochemical Cycling: Separation of Reversible and Irreversible Heat Effects». In: *Batteries* 6 (2020) (cit. on p. 59).

Acknowledgements

Per concludere, vorrei ringraziare le persone che hanno permesso la realizzazione di questo lavoro e che sono state al mio fianco durante questi anni di studio.
In primis, ringrazio i prof. Massimo Santarelli e Silvia Bodoardo per avermi dato l'opportunità di fare questa bellissima esperienza e di lavorare in uno splendido ambiente. Inoltre, ci tengo a ringraziare Davide Dessantis, senza il suo aiuto questo lavoro non avrebbe visto la luce. Grazie per essere stato così paziente e per il tempo che mi hai dedicato. Ringrazio anche tutto il gruppo di elettrochimica, per tutto l'appoggio che mi avete dato quando ne avevo bisogno.
I miei più grandi ringraziamenti vanno alla mia famiglia, i pilastri della mia vita, senza di loro non avrei mai potuto raggiungere questo traguardo. Grazie per avermi tirata su quando pensavo di non farcela e per aver sempre creduto nelle mie capacità. Ringrazio mia sorella per avermi sempre spronata, spero di riuscire a fare altrettanto io.
Ringrazio Marco, senza il cui sostegno e forza non avrei superato neanche un esame. Grazie per tutte le volte che mi hai consolata, per essere riuscito tutte le volte a dare la giusta proporzione alle mie mille preoccupazioni e per non avermi mai fatto perdere di vista i veri obiettivi della vita. In parte i miei successi sono dovuti a te.
Vorrei ringraziare le mie amiche di sempre Sara, Veronica ed Eleonora. Grazie per il vostro supporto e per avermi dato ad ogni esami tutta la carica di cui avevo bisogno. Vi ho sempre sentite vicine, nonostante i km che ci separavano. Ognuna di noi sa che potremo sempre contare sull'appoggio dell'altra, nonostante la distanza e nonostante gli impegni. Voi verrete sempre prima di tutto. Grazie perché con voi non devo trasformarmi in qualcosa che non sono, quello che sono per voi è già prezioso così com'è.
Ringrazio i miei mitici compagni di studio, Valeria, Arianna, Giovanni e Riccardo

per le mille risate insieme e per aver reso il Politecnico un posto molto più leggero. In particolare, ci tengo a ringraziare Valeria per l'infinita positività che sa trasmettere. Lavorare con te mi ha aiutata a crescere e a migliorarmi. Se oggi affronto le cose in maniera diversa, con maggiore tranquillità e consapevolezza del mio potenziale questo è merito tuo. Sei il mio girasole [cit.].
Ringrazio il mio secondo girasole, Chiara. Il nostro rapporto è quello che più di tutti mi ha messo alla prova e mi ha fatto crescere. Partito decisamente non nel migliore dei modi, entrambe con le nostre insicurezze e il bisogno di sentirci accettate per quello che siamo. Ho trovato molto di me in te ed è stato questo probabilmente a legarci. Spero per sempre.
Inoltre, ci tengo a ringraziare Cristina. Tu e Chiara siete come sorelle per me. Con te ho condiviso ansie, frustrazioni e gioie, sapevo di poter essere sempre capita perché quello che provavo io lo stavi vivendo anche tu. Niente potrà cambiare il bene che ti voglio.
Ringrazio inoltre Francesca, Agnese, Antonio, Carmelo e Piergiorgio, vi voglio bene.